

Article

Experimental Investigation of the Hydrodynamic Performance of Land-Fixed Nearshore and Onshore Oscillating Water Column Systems with a Thick Front Wall

Ayrton Alfonso Medina Rodríguez ^{1,*}, Gregorio Posada Vanegas ^{2,†}, Rodolfo Silva Casarín ^{1,†}, Edgar Gerardo Mendoza Baldwin ^{1,†}, Beatriz Edith Vega Serratos ^{2,†}, Felipe Ernesto Puc Cutz ^{2,†} and Enrique Alejandro Mangas Che ^{2,†}

¹ Institute of Engineering, National Autonomous University of Mexico, Circuito Escolar, Mexico City 04510, Mexico; RSilvaC@iingen.unam.mx (R.S.C.); emendozab@iingen.unam.mx (E.G.M.B.)

² EPOMEX Institute, Autonomus University of Campeche, 480 Héroe de Nacozari Ave, Campeche 24079, Mexico; gposadav@uacam.mx (G.P.V.); beavega@uacam.mx (B.E.V.S.); feliepuc@uacam.mx (F.E.P.C.); al035699@uacam.mx (E.A.M.C.)

* Correspondence: ayrtonamedinar@gmail.com

† These authors contributed equally to this work.



Citation: Medina Rodríguez, A.A.; Posada Vanegas, G.; Silva Casarín, R.; Mendoza Baldwin, E.G.; Vega Serratos, B.E.; Puc Cutz, F.E.; Mangas Che, E.A. Experimental Investigation of the Hydrodynamic Performance of Land-Fixed Nearshore and Onshore Oscillating Water Column Systems with a Thick Front Wall. *Energies* **2022**, *15*, 2364. <https://doi.org/10.3390/en15072364>

Academic Editors:
Mohamed Benbouzid and
Elhoussin Elbouchikhi

Received: 5 January 2022

Accepted: 17 March 2022

Published: 24 March 2022

Publisher's Note: MDPI stays neutral with regard to jurisdictional claims in published maps and institutional affiliations.



Copyright: © 2022 by the authors. Licensee MDPI, Basel, Switzerland. This article is an open access article distributed under the terms and conditions of the Creative Commons Attribution (CC BY) license (<https://creativecommons.org/licenses/by/4.0/>).

Abstract: Most experimental research on land-fixed Oscillating Water Column (OWC) systems assume that the OWC-water wave interaction happens with waves that propagate normally towards the device. However, the angle of incidence of the waves can determine the performance of the OWC, in particular the wave period at which the device resonates. In this study, an experimental investigation to examine the interaction of regular, oblique, water waves with a land-fixed, thick-front wall OWC device in terms of its hydrodynamic performance is reported. A 1:20 Froude scale was used to replicate a single chamber of the Mutriku Wave Energy Plant (MWEP), and a series of tests were carried out in a spectral wave basin. The goal of this study is to look at how incident wave direction and device location affect the hydrodynamic performance of land-fixed OWC systems in regular wave conditions with varying wave heights. The hydraulic performance includes the assessment of the wave amplification factor, hydrodynamic efficiency, the non-dimensional air pressure inside the chamber and non-dimensional water pressures on the chamber walls. The findings show that, for the nearshore OWC device, the period at which resonance occurs decreases when the incident wave angle increases. For the corresponding wave angles, similar results were found for the onshore and nearshore OWC devices, with a slight frequency shift in the bandwidth of the hydrodynamic efficiency. Furthermore, it was found that when wave height increases, the hydrodynamic efficiency improves for both short and long wave periods, with the exception of the resonance period, where the trend is reversed. Finally, regardless of the location, an OWC device with a thick front wall performs well when interacting with intermediate and long-period waves.

Keywords: wave energy conversion; oscillating water column; wave energy converter; wave basin; oblique waves; hydrodynamic performance

1. Introduction

The accelerating growth of the human population and the negative impact of fossil fuel exploitation on the global climate has triggered an increasing need for renewable energy. Sustainable and clean, renewable energy is derived from nature, is regenerative and does not deplete over time [1]. Among the different options of renewable energies, marine energy has a promising future, considering that more than 70% of the earth's surface is seawater and that there are various options (waves, tides, currents, thermal gradients and saline gradients) [2]. In this regard, ocean-wave energy has the advantage of having a higher energy flow density and higher spatial concentration compared with

other renewable energy sources, and of being generally predictable, with limited negative environmental impacts when used [3,4].

In recent years several nations have devoted time and resources to the study and development of extraction technologies for ocean-wave energy harvesting. More than a thousand patents had been registered by the 1980s, and the number has grown significantly since then [5]. A detailed overview of existing concepts and designs is available in [6–8]. These wave energy converters (WECs) capture wave energy and transform it into another type of energy (generally electricity). The Oscillating Water Column (OWC) device stands out among the many types of WECs because of its simplicity and adaptability. As a result, OWCs have been installed and tested in a diversity of locations. The OWC system consists of a partially submerged capturing chamber, which is opened at the bottom to allow the water to flow inside. An air column is trapped in the upper part of the collecting chamber and the free water surface oscillations compress and decompress the air in the upper part of the chamber. Compressed air is forced into a power take-off, or PTO, consisting of an air turbine and an electric generator [9].

OWC systems have advantages over other existing WECs because:

- In particular, the convenience and safety of access for installation and maintenance to the power plant make it more convenient for coastal and near-shore devices, as well as eliminating the need for mooring systems and subsea power cables.
- Gearboxes are not required because an air turbine is used.
- Construction and maintenance become more available when they are planned to be erected on the shore or as part of pre-existing ocean structures [10].
- In particular, access to the power plant becomes more convenient for coastal and nearshore devices, and it eliminates the need for mooring systems and undersea electric cables.

However, coastal and nearshore systems, which are the focus of this work, have a number of drawbacks, including lesser wave power due to shallow water, significant tidal range, site-specific requirements of their location such as shoreline bathymetry, preservation of coastal scenery, recreation activities and wave energy distribution, which means devices cannot be mass-produced [3,11].

Worldwide, several full-sized fixed OWC systems have been tested, such as in Toftestallen, Norway (500 kW), Sakata in Japan (60 kW), Vizhinjam in India (150 kW), Pico in Portugal (400 kW), Limpet in Scotland (500 kW) and the Mutriku Wave Energy Plant (MWEP) in Spain (300 kW) [12]. The OSPREY was the largest of them, but it was destroyed by the sea shortly after being pulled into position on the Scottish coast [13]. At present, the MWEP is most likely the only commercial land-fixed OWC wave farm that is consistently producing power to the grid [14]. Whilst the deployment of multiple full-sized systems has generated interest around the world, fixed OWC technology has yet to be commercialised completely. Therefore, further hydrodynamic research on land-fixed OWC devices is needed to increase their reliability and survivability [15,16].

OWC performance has drawn the attention of many researchers since the 1970s, all hoping to achieve maximum energy absorption [17]. Experimental tests were conducted by Morris-Thomas et al. [18] to examine the hydrodynamic efficiency of a shore-based OWC device. They found that the overall shape and bandwidth of the hydrodynamic efficiency curve are influenced by the front wall geometry. Torre-Enciso et al. [19] conducted an experimental evaluation on the performance of an array of OWC devices coupled with a caisson breakwater. Although the main idea behind the construction of the caisson breakwater was to protect the harbour, it led to the development of the Mutriku wave power plant, the world's first commercial OWC plant [14]. Ikoma et al. [20] investigated the effects of an artificial harbour attached to an OWC device to improve the primary conversion efficiency. Lopez et al. [21] analysed the influence of the wave conditions, turbine damping and tidal level on the efficiency of an OWC device. The authors highlighted the importance of coupling the turbine and the OWC chamber, having found that the damping exerted by the turbine was the main influence on system efficiency, even more than the wave

conditions. Ashlin et al. [22] conducted a series of experiments in a wave flume to quantify the horizontal and vertical wave forces on a scaled OWC model. They observed that at the natural frequency of the system, the force on the OWC structure is lower, due to the high-energy absorption of the system.

Ashlin et al. [23] tested four different bottom profiles (flat, circular curve and two slopes) to evaluate their effects on the hydrodynamic performance of the OWC. They found that the circular curve bottom profile gave a better performance in terms of wave energy conversion and wave amplification factor inside the chamber. Ashlin et al. [24] investigated the performance of an array of OWC devices integrated with an offshore detached breakwater exposed to oblique wave incidence through experiments. They found that when the wave angle is less, the performance of the system decreases because the wavefront hits the system at different times, while the natural frequency of the system remains the same. Experimental tests to evaluate the effects of the incident wave amplitude and the OWC geometric parameters on the hydrodynamic efficiency were carried out by [15]. They concluded that the amplitude of the incoming wave does not affect the resonance frequency or the hydrodynamic efficiency.

Rezanejad et al. [25] carried out an experimental campaign with both regular and irregular waves to investigate the influence of the incident wave parameters and the turbine damping on the efficiency of an OWC device. Howe and Nader [26] evaluated the hydrodynamic response of two types of Bent Duct OWC devices, in isolation and when combined with a flat-faced breakwater. The authors discovered that by incorporating a bent duct OWC WEC into a marine structure, such as a harbour or breakwater, the extraction efficiency of the device might be significantly improved. Ashlin et al. [27] carried out an experimental campaign to study the effect of different spacings in an array of OWC devices integrated with an offshore detached breakwater. They found that an array of OWC devices has a better performance than an isolated system. Rezanejad et al. [28] used both experimental and numerical techniques to investigate the primary efficiency of an OWC device in a stepped sea bottom condition. They concluded that the primary efficiency of the system is mostly influenced by the wave period in regular waves and that the variation in wave height has an impact on performance, particularly in short wave periods. The impact of air compressibility on the capture width ratio of land-fixed OWC devices was experimentally investigated by [29]. The authors stated that ignoring air compressibility may lead to either under- or over-predictions of power output. Çelik and Altunkaynak [30] performed experimental and numerical free decay tests to investigate the effect of the height of various underwater openings and power take-off (PTO) mechanisms in a stationary OWC device. Chen et al. [31] studied the correlation of the optimal chamber width with the relative front wall draught of an onshore OWC device. They determined that the highest energy conversion efficiency of the OWC system occurs at a phase difference of around one-quarter of the wave period between the water surface fluctuations inside and outside the chamber.

In this work, a scaled thick front wall OWC device was studied in a directional wave basin for two different experimental configurations; testing nearshore and onshore locations. Nearshore devices are deployed in relatively shallow water conditions, usually at a depth of less than one-quarter the wavelength [3]. They absorb wave energy close to shore, which is converted to electricity in an onshore plant. Nearshore devices are frequently anchored, or fixed, to the seafloor, providing a suitably stable basis versus which an oscillating body can function. The main disadvantage of this sort of device is the lower wave power found in shallow water, which reduces their harvesting capability [3].

On the other hand, onshore devices that are attached to the coastline share the advantages of nearshore devices and both are simple to install and maintain. Anchors and specialized infrastructure are unnecessary, and the storm damage is likely to be negligible [32], although still possible, as demonstrated in the MWEP [33]. Furthermore, extensive electrical cables under the sea are not required to get the electrical energy to the coast. Because onshore wave energy devices are typically placed near existing infrastructure,

development, installation, power transfer, and maintenance costs can be significantly less than for offshore wave power generators. However, as with nearshore devices, the onshore environment has less wave energy flow and lower potential [34].

As previously stated, most research has concentrated on the 2D interaction between water waves and land-fixed OWC devices with a thin front-wall. However, under real sea conditions, land-fixed OWC systems cannot really be built with a thin front wall. This is because land-fixed OWC devices are expected to be stable and structurally safe and in periods with high water levels they will be subjected to extreme forces from direct wave action. Furthermore, OWC devices are meant to function as a terminator device, with their principal axis perpendicular to the prevailing wave direction in order to collect the greatest energy, although this seldom occurs in practise [35]. For example, the incident water waves impacting the MWEF combined OWC-breakwater system are generally oblique [14], and the front wall is thick to enable the system to withstand high wave conditions [33]. To complement previous research on land-fixed OWCs, and motivated by the case of the MWEF, the objective of this paper is to focus on the effect of incident wave direction on the hydrodynamic performance of both nearshore and onshore land-fixed OWC devices under regular wave conditions with different wave heights.

The work is organized as follows: Section 2 describes the test facility, scaled model, the instrumentation employed in the experiments and the experimental set-up. A description of the dimensional analysis, hydrodynamic efficiency and other hydrodynamic quantities of interest are presented in Section 3. Section 4 presents the results and discussion for the nearshore and onshore OWC devices. Finally, in Section 5, the main conclusions of the study are drawn.

2. Experimental Campaign

2.1. Test Facility

The experimental campaign was carried out in the directional wave basin of the Autonomous University of Campeche, Mexico, which is 15 m long, 9 m wide, and 0.8 m deep. The wave basin is equipped with a linear snake type wavemaker of 18 piston paddles 50 cm wide each. The equipment features an active absorption system. An artificial beach at the other end of the basin serves as a passive wave absorber, is made of gravel $D_{50} = 5.08$ cm and has an average weight of 54 g. Schematic views of the directional wave basin showing the position of eight wave gauges and the two models tested are shown in Figure 1a,b. The nearshore OWC model was positioned 5.62 m from the wavemaker, while the onshore OWC model was positioned at the beginning of the sloped artificial beach.

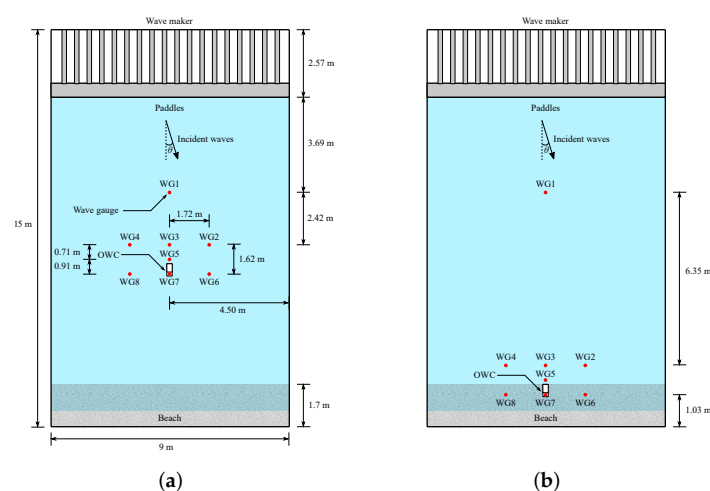


Figure 1. Schematic plan view of the directional wave basin and the experimental set-up. (a) Experimental set-up for the nearshore Oscillating Water Column (OWC) device. (b) Experimental set-up for the onshore OWC device.

2.2. Test Model

A line scale of 1:20 under Froude similarity law was chosen for modelling the OWC chamber. Froude's similarity was used because it allows to represent an equivalent OWC system between the model and full scale with the same vertical and horizontal length scales, thus being geometrically identical. The scale ratio ($\Lambda = 20$) was chosen based on the size of the experimental facilities, as well as the wave conditions examined. However, when applying Froude similarity, other force-to-force ratios, such as inertia to surface tension, inertia to viscosity, and inertia to compressive forces, are distorted [21]. Viscous forces, are often not significant over the short distances modelled, and surface tension effects are generally insignificant for models with water depths and wave periods greater than 20 mm and 0.35 s, respectively [36]. The remaining potential scale effects are the compressive forces, which are present in the aerodynamic phase that activates the PTO [37], but are insignificant in the hydrodynamic phase since water compressibility is minimal even at small scales. In small scale testing, achieving the combined hydrodynamic and aerodynamic scaling requirements would be complicated [38] and would require impractical alterations to the fluid density or the atmospheric pressure. One way to achieve this would be to scale the volume of the air chamber (V) in accordance to the square of the length scale ratio ($V \propto \Lambda^2$) [39]. The OWC chamber can then be scaled via Froude's similitude law ($V \propto \Lambda^3$) and an air reservoir be added to provide the air volume deficit determined by the square scale factor and thus avoid ignoring the effects of the air compressibility on the performance of the OWC model [40]. With these considerations, the Froude similitude requirement is fulfilled in the hydrodynamic domain to achieve full geometric similarity between the model and prototype devices, while the air chamber and an additional air reservoir can help satisfy the ratio of inertia forces to air compression forces. However, following [21], in this study only the geometric similarity conditions were fully met, which is a useful approach to hydrodynamically characterise the performance of an OWC in its early stages of development. However, when a thorough examination of the performance is necessary, this approach might lead to incorrect estimations of the hydrodynamic efficiency.

Figure 2a,b show the dimensional details of the OWC model in front and plan views, as well as cross-sectional elevation. The OWC chamber has a length (b) of 155 mm, a width (d) of 225 mm and height (L_1) of 655 mm, see Figure 2a. The front wall draft (a) and thickness (w) were 260 mm and 333 mm, respectively. The OWC model was made of acrylic sheets, with a thickness of 12 mm and cut with a laser system. The water depth (h) was 400 mm, kept constant throughout all the experiments. The gap (B_g) below the front wall was 140 mm. To ensure the rigidity of the OWC device, five additional weights (8 kg) of lead were used. The distance between the beach and the nearshore OWC model was fixed as 3.0 m. For the onshore set-up, the same OWC model was employed, but placed in line with the artificial beach of 1.70 m length and 0.54 m height, see Figure 2b. Since the line scale is too small for a turbine to be adequately simulated, the PTO was simulated by an orifice to apply the equivalent resistance of a self-rectifying impulse turbine [39]. The reason is that pressure drop across the orifice varies quadratically with the flow rate, as it does across an impulse turbine [21]. Early developments in OWC technology focused on Wells turbines. However, over the recent years research has been mainly directed toward impulse turbines. Hence, an impulse turbine was selected in this study as the PTO unit acting on the OWC system. The PTO damping on the OWC chamber is represented by a circular air hole, where the opening ratio of the air hole area to the waterplane area of the OWC chamber (χ) was 0.68%. Previous investigations have reported that OWC devices achieve their best performances mainly when the orifice area is around 1% of the cross-sectional area of the OWC model. Ashlin et al. [23] found that the best energy absorption is obtained when the orifice area is about 0.68% of the OWC area; therefore, this ratio was that used, and it was kept constant throughout the tests of the present investigation.

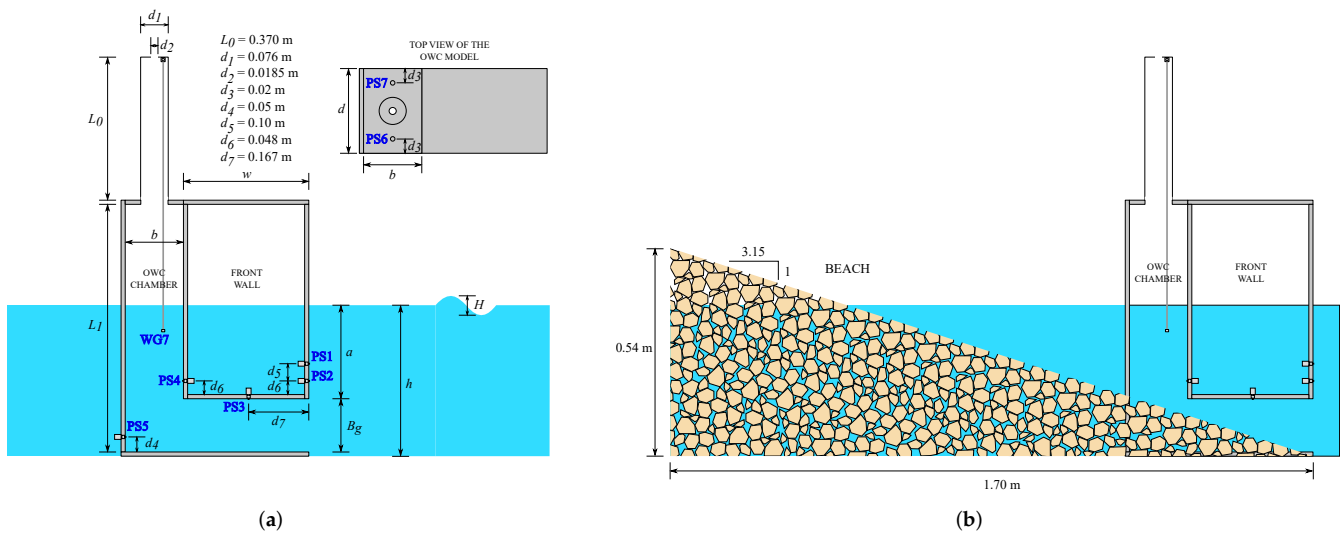


Figure 2. Vertical cross section of the experimental set-up. (a) Dimensional details of OWC model. (b) Dimensional details of the artificial beach.

Views of the model setup for nearshore and onshore land-fixed devices, the absorbing beach and the wavemaker are seen in Figure 3a,b. The OWC dimensions are based on a single, thick front wall OWC chamber of the MWEF [41,42]. It should be noted that in this work only a single wall thickness was investigated.

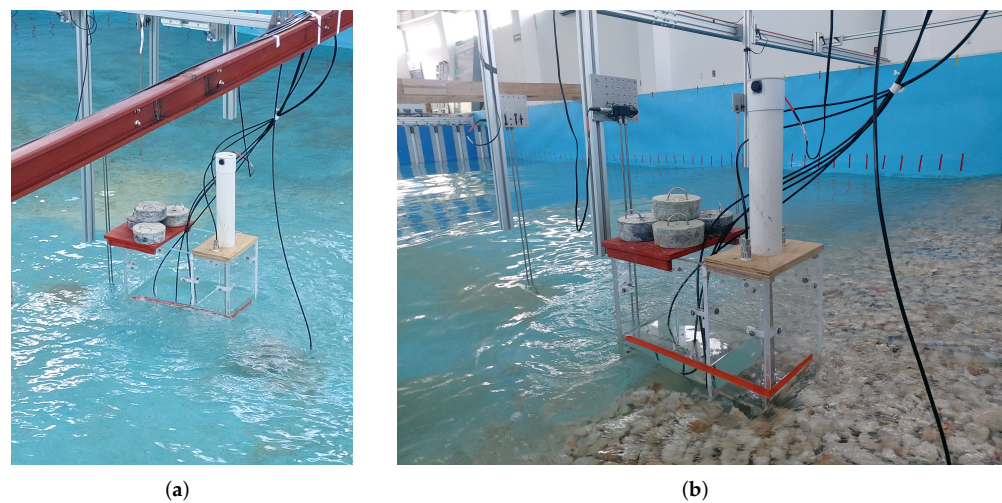


Figure 3. The experimental set-up of the land-fixed OWC. (a) Nearshore OWC device. (b) Onshore OWC device.

2.3. Instrumentation

To record water-free surface elevations outside the OWC model, seven resistance type wave gauges were installed within the wave basin. Five of these gauges were located in front of the OWC model, and the remaining two were mounted at 1.72 m from the lateral sides of the model, as shown in Figure 1a,b. One resistance wave gauge was installed inside the chamber of the model (in the middle) as well as seven air pressure gauge sensors. The sampling frequency of all the sensors was 100 Hz. A WG1 sensor was installed to detect the incident wave pattern at the beginning of each test. The data measured by wave gauges WG2 and WG4 were compared with the measurements of the WG3, while wave gauges WG6 and WG8 were compared with the measurements of WG7.

The seven pressure transducers used to register the air pressure variation have a measuring range of 0.3 bars. Two were placed in the front wall of the OWC chamber, facing the waves (PS1 and PS2); one in the lower face of the front wall (PS3); another in the inner side of the front wall (PS4); one in the lower part of the back wall (PS5); and two inside the chamber at the top (PS6 and PS7). The differential air pressure measured by PS6 and PS7, and the chamber free surface elevation by WG7, were adopted to calculate the efficiency of the system. The analysis of the measurements was executed in the time window of the steady-state region (i.e., the time-series window without start-up time and reflection).

2.4. Experimental Set-Up

The OWC device was tested under regular wave conditions. Details of the experimental conditions are summarized in Table 1. To thoroughly characterise the performance of the OWC, a total of 165 regular wave conditions were tested, resulting from the combination of five wave heights, from $H = 0.02$ m to $H = 0.10$ m, in increments of 0.02 m (from $H = 0.04$ m to $H = 2.0$ m, in full-scale dimensions), eleven wave periods, from $T = 1.0$ s to $T = 3.0$ s, in increments of 0.2 s (from $T = 4.47$ s to $T = 13.42$ s, in full-scale dimensions) and three incident wave angles from $\theta = 0^\circ$ to $\theta = 30^\circ$, in increments of $\theta = 15^\circ$. These wave conditions were tested for nearshore and onshore OWC configurations; however, the results for $\theta = 30^\circ$ in the onshore OWC model are not shown, since the effect of the reflection generated by the lateral wave basin walls was significant. In total, the experimental campaign comprised 275 tests, each with a duration of 300 s.

Table 1. Test conditions and geometric parameters of the Oscillating Water Column (OWC) model.

Parameter	Value or Range
Water depth (h)	0.4 m
Incident wave height (H)	0.02–0.10 m at 0.02 m interval
Wave period (T)	1.0–3.0 s at 0.2 s interval
Wave length (λ)	1.464, 1.936, 2.393, 2.836, 3.269, 3.695, 4.115, 4.532, 4.945, 5.356 and 5.765 m
Model length (b)	0.155 m
Model width (d)	0.255 m
Model height (L_1)	0.655 m
Model draft (a)	0.260 m
Model front wall thickness (w)	0.333 m
Gap length (B_g)	0.128 m

3. Hydrodynamic Parameters

3.1. Dimensional Analysis

Following He and Huang [43], for an OWC model, the extracted wave power (P_{out}), the amplitude of the surface displacement and the fluctuation in pressure inside the chamber (η_{owc} and Δp , respectively) are mainly affected by the following variables: the OWC model length (b), width (d), draft (a), the thickness of the front wall (w), the opening ratio (χ), the period of incident waves (T), the height of incident waves (H), the water depth (h), the water density (ρ), and the gravitational acceleration (g), while the effects of the kinetic viscosity of the water can be disregarded since the Reynolds number is large. Therefore,

$$\eta_{owc}, \Delta p, P_{out} = f(b, d, a, w, \chi, T, H, h, \rho, g), \quad (1)$$

and after a dimensional analysis, we obtain

$$\left(\frac{\eta_{owc}}{H}, \frac{\Delta p}{\rho g H}, \frac{P_{out}}{P_{in}} \right) = f \left(\frac{b}{h}, \frac{d}{b}, \frac{a}{h}, \frac{w}{b}, \chi, \frac{H}{h}, T \sqrt{\frac{g}{b}} \right). \quad (2)$$

Then, we define the following dimensionless parameters

$$\alpha = \frac{\eta_{owc}}{H}, \quad (3a)$$

$$\bar{P} = \frac{\Delta p}{\rho g H}, \quad (3b)$$

$$\epsilon = \frac{P_{out}}{P_{in}}, \quad (3c)$$

where the extracted wave power P_{out} is explained in detail in Section 3.2 and the available power over one wave period of a monochromatic wave is given by

$$P_{in} = E c_g \quad (4)$$

with E being the total energy per wave period and c_g the group velocity given by

$$E = \frac{1}{2} \rho g w \left(\frac{H}{2} \right)^2, \quad (5)$$

$$c_g = \frac{1}{2} \frac{\omega}{k} \left(1 + \frac{2kh}{\sinh(2kh)} \right), \quad (6)$$

respectively, where k represents the wave number that satisfies the dispersion relation given by

$$\omega^2 = gk \tanh(kh), \quad (7)$$

and ω is the angular frequency of the waves.

The dimensionless parameters b/h , d/b , a/h , w/b and χ were held constant in our experiments. Equation (2) can thus be reduced to

$$(\alpha, \bar{P}, \epsilon) = f \left(\bar{H} = \frac{H}{h}, \bar{T} = T \sqrt{\frac{g}{b}} \right), \quad (8)$$

which means that our findings can be presented with only these two dimensionless parameters. Details of the values of these dimensionless parameters are given in Table 2.

Table 2. Varying non-dimensional parameters for the experimental tests.

Parameter	Value or Range
Relative wave height (\bar{H})	0.05, 0.10, 0.15, 0.20 and 0.25
Relative wave period (\bar{T})	7.956, 9.547, 11.138, 12.729, 14.320, 15.911, 17.502, 19.093, 20.684, 22.275 and 23.867

3.2. Hydrodynamic Efficiency

The main hydrodynamic parameter used to evaluate the system performance is hydrodynamic efficiency. This can be evaluated by estimating the incident wave power and the power absorbed from waves. The average power absorbed from regular waves P_{out} can be determined by integration of the instantaneous free surface oscillation inside the chamber moving with a velocity (V_{fs}) under the air pressure (ΔP) as follows

$$P_{out} = \frac{1}{T_{end} - T_{ini}} \int_{T_{ini}}^{T_{end}} \Delta P S_{chamber} V_{fs} dt, \quad (9)$$

where T_{ini} and T_{end} are the initial and final times in the steady state region of the measurements; $S_{chamber} = b \times d$ is the water plane area of the OWC chamber; and t is the time. The airflow can be assumed to be an incompressible flow due to the small volume of air trapped

inside the model [44]. Thus, V_{fs} can be estimated by calculating the first time derivative of the third-order approximation to the free surface elevation inside the OWC chamber [21] as

$$V_{fs} = \frac{2\eta_{j+1} + 3\eta_j - 6\eta_{j-1} + \eta_{j-2}}{6\Delta t}, \quad (10)$$

where η_j is the elevation of free surface at time t_j , j is the current time value and Δt is the sampling interval. Furthermore, it should be mentioned that the air pressure within the chamber ΔP is calculated by means of averaging the data gathered from the two pressure gauges (PS6 and PS7) at each time instant.

3.3. Dimensionless Hydrodynamic Quantities

In order to study the influence of the dimensionless parameters, H/h and h/λ on the pressures that are exerted in the chamber, the following dimensionless quantities are defined

$$P_{fwout} = \frac{\Delta P_{PS2}}{\rho g H}, \quad (11a)$$

$$P_{fwbottom} = \frac{\Delta P_{PS3}}{\rho g H}, \quad (11b)$$

$$P_{fwin} = \frac{\Delta P_{PS4}}{\rho g H}, \quad (11c)$$

$$P_{bw} = \frac{\Delta P_{PS5}}{\rho g H} \quad (11d)$$

and

$$P_{chamber} = \frac{\Delta P_{PS6 \text{ and } PS7}}{\rho g H}, \quad (11e)$$

where ΔP represents the difference between the maximum and minimum pressures measured by the pressure gauges in the time window of the steady-state region. It should be noted that the pressure recorded by PS1 is not presented here owing to its similarity with the data collected by PS2. Finally, the volume flow rate $Q = S_{chamber} \cdot V_{fs}$ is also determined and normalized by " $bdH\omega$ " to represent the dimensionless volume flow rate \bar{Q} and evaluate the phase difference between this quantity and the air pressure within the chamber.

4. Results and Discussion

4.1. Nearshore OWC Model

In this subsection, the experimental results of the nearshore OWC model (Figure 1a) are shown. The wave amplification factor, hydrodynamic efficiency and air pressure inside the OWC chamber for different wave heights and incidence wave angles are presented and discussed. Additional findings for the pressure on the walls of the OWC chamber are presented in Appendix A.

4.1.1. Amplification Factor

The wave amplification factor α is shown in Figure 4a–c with $\theta = 0^\circ$, 15° and 30° for the nearshore OWC model. Figure 4a–c show that the wave amplification factor increases as the non-dimensional wave height \bar{H} decreases, except for large values of \bar{T} , i.e., for long wavelengths. It is also seen in these figures that the smaller \bar{H} , the larger the effective area under the amplification factor curve. Moreover, α reaches the resonance condition for medium values of the non-dimensional wave period \bar{T} around 14.32 and 17.50 s. Thus, for a nearshore full-scale OWC device with the dimensions and conditions proposed in this work, the required incident wave periods for a maximum amplification will be in the

range of 8 and 10 s. The fact that small wave periods do not generate maximum elevation of the free surface inside the chamber is explained by the fact that for a thick front wall, the transfer of energy due to the orbital motion of high-frequency waves (i.e., small \bar{T}) is less, and the lip wall prevents the wave energy from entering the chamber, while the reflected energy increases. Contrary to results reported by [24] where the wave amplification factor is higher for a normal angle of incidence of the wave, due to the absence of obstruction and energy dissipation, we did not observe a clear trend between 0–15° and 15–30°. Although there appeared to be a slightly increasing tendency from 0° to the 15° for each wave height, this trend is not observed between 15° to 30°. Perhaps, this result is related to the use of a single resistance wave gauge within the OWC chamber.

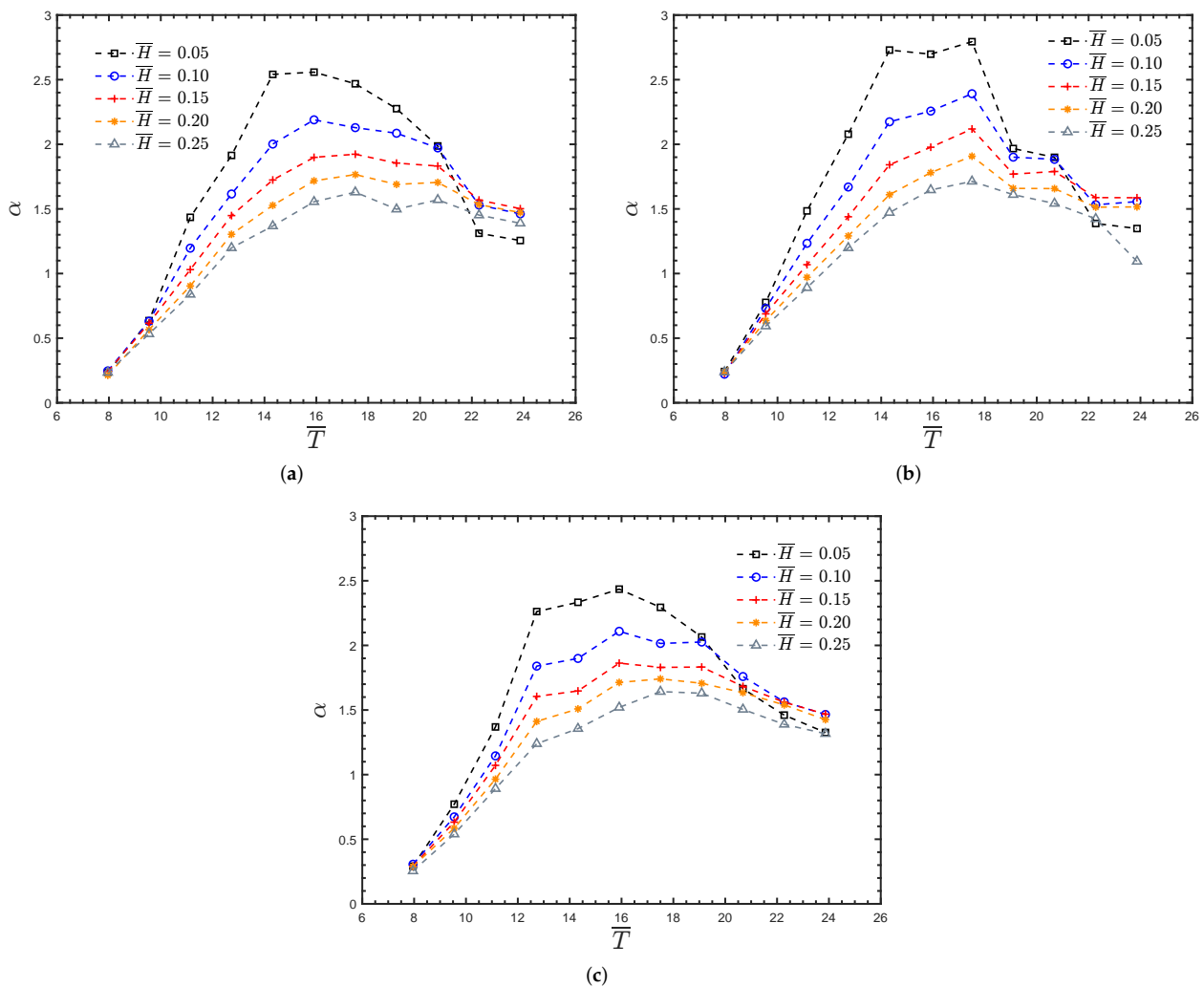


Figure 4. Variation of amplification factor α versus \bar{T} for the nearshore OWC model. (a) Amplification factor α versus \bar{T} with $\theta = 0^\circ$ for the nearshore OWC model. (b) Amplification factor α versus \bar{T} with $\theta = 15^\circ$ for the nearshore OWC model. (c) Amplification factor α versus \bar{T} with $\theta = 30^\circ$ for the nearshore OWC model.

4.1.2. Hydrodynamic Efficiency

The hydrodynamic efficiency ε versus the non-dimensional wave period \bar{T} for different incident wave angles θ (0°, 15° and 30°) and various non-dimensional wave heights \bar{H} is shown in Figure 5a–c. In these figures, it is seen that the bandwidth of the curves increases when \bar{H} increases. It is also observed that for intermediate wave periods, where the peak values are observed, the hydrodynamic efficiency decreases when \bar{H} increases, around 50% between $\bar{H} = 0.25$ and 0.05. However, in the long and short wave period

regimes, the hydrodynamic efficiency increases when \bar{H} also increases. These findings are consistent with those found by [25] for a high damping condition exerted on the system by the model PTO, and therefore the decreasing trend in efficiency approaching resonance may be attributed to non-linear processes linked with increased water sloshing and free surface deformation caused by large wave heights [45]. Therefore, we can conclude that increasing the wave height enhances the performance of the proposed OWC device for small non-dimensional wave periods $\bar{T} < 11$ and large wave periods $\bar{T} > 19$, regardless of the wave angles. Nonetheless, the non-dimensional wave height \bar{H} does not influence the value of the non-dimensional wave period at which resonance occurs, while the wave direction does. In Figure 5a,b it is seen that resonance occurs at $\bar{T} = 14.32$ ($T = 1.8$ s), while in Figure 5c it occurs at $\bar{T} = 12.73$ ($T = 1.6$ s), which are smaller compared to those in α . Thus, our results cast a new light on the effect of wave direction on land-fixed OWC performance, since this aspect can affect the value of the resonance period at which maximum hydrodynamic efficiency occurs, while the combination of large periods and wave heights may be beneficial to increase the hydrodynamic efficiency.

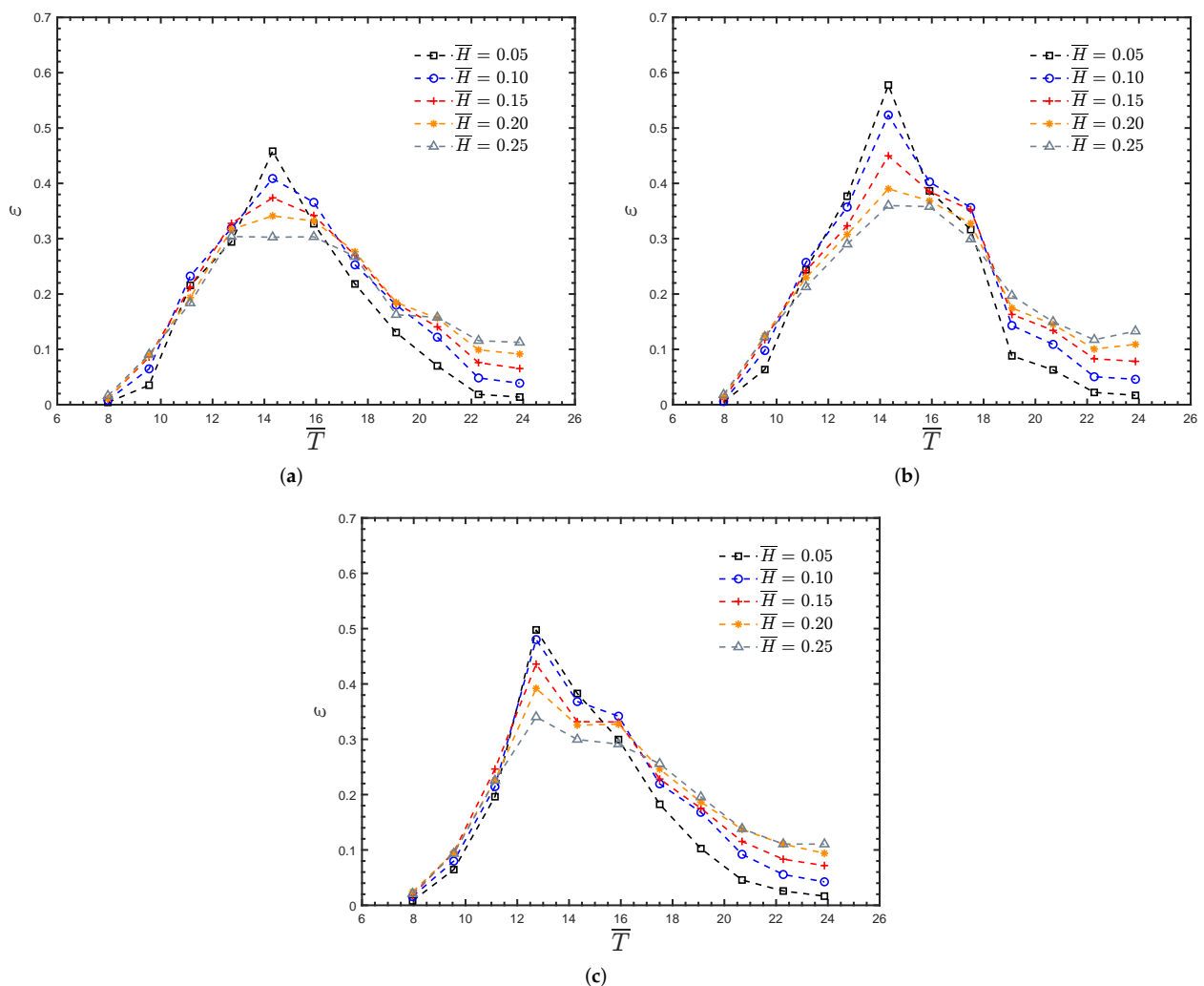


Figure 5. Hydrodynamic efficiency ϵ versus \bar{T} for the nearshore OWC model. (a) Hydrodynamic efficiency ϵ versus \bar{T} with $\theta = 0^\circ$ for the nearshore OWC model. (b) Hydrodynamic efficiency ϵ versus \bar{T} with $\theta = 15^\circ$ for the nearshore OWC model. (c) Hydrodynamic efficiency ϵ versus \bar{T} with $\theta = 30^\circ$ for the nearshore OWC model.

4.1.3. Non-Dimensional Air Pressure

The average non-dimensional air pressures inside the OWC chamber $P_{chamber}$ versus the non-dimensional wave period for various non-dimensional wave heights \bar{H} with $\theta = 0^\circ$, 15° and 30° are shown in Figure 6a–c. These figures show that the values in $P_{chamber}$ increase when the non-dimensional wave height \bar{H} increases. This also leads to an increase in the bandwidth of the $P_{chamber}$ curves. Contrary to the trend observed in wave amplification, air pressure is higher for longer wave periods and higher wave heights, which improves the OWC hydrodynamic performance, Figure 5a–c. It is seen that the peak values of $P_{chamber}$ occur at $\bar{T} = 14.32$, i.e., $T = 1.8$ s for $\theta = 0^\circ$ and 15° , while for 30° it occurs at $\bar{T} = 12.73$, i.e., $T = 1.6$ s, which coincide with the hydrodynamic efficiency ε in Figure 5a–c. As observed numerically by [46], both the maximum wave amplification factor (α) and air pressure inside the chamber ($P_{chamber}$) do not occur with the same wave period. On one hand, the maximum α occurs at longer wave periods, since energy transmission into the chamber due to the orbital motion is larger, while maximum air pressure and hydrodynamic efficiency, Figure 5a–c, occur with the resonant period of the chamber when the air volume flux is maximum.

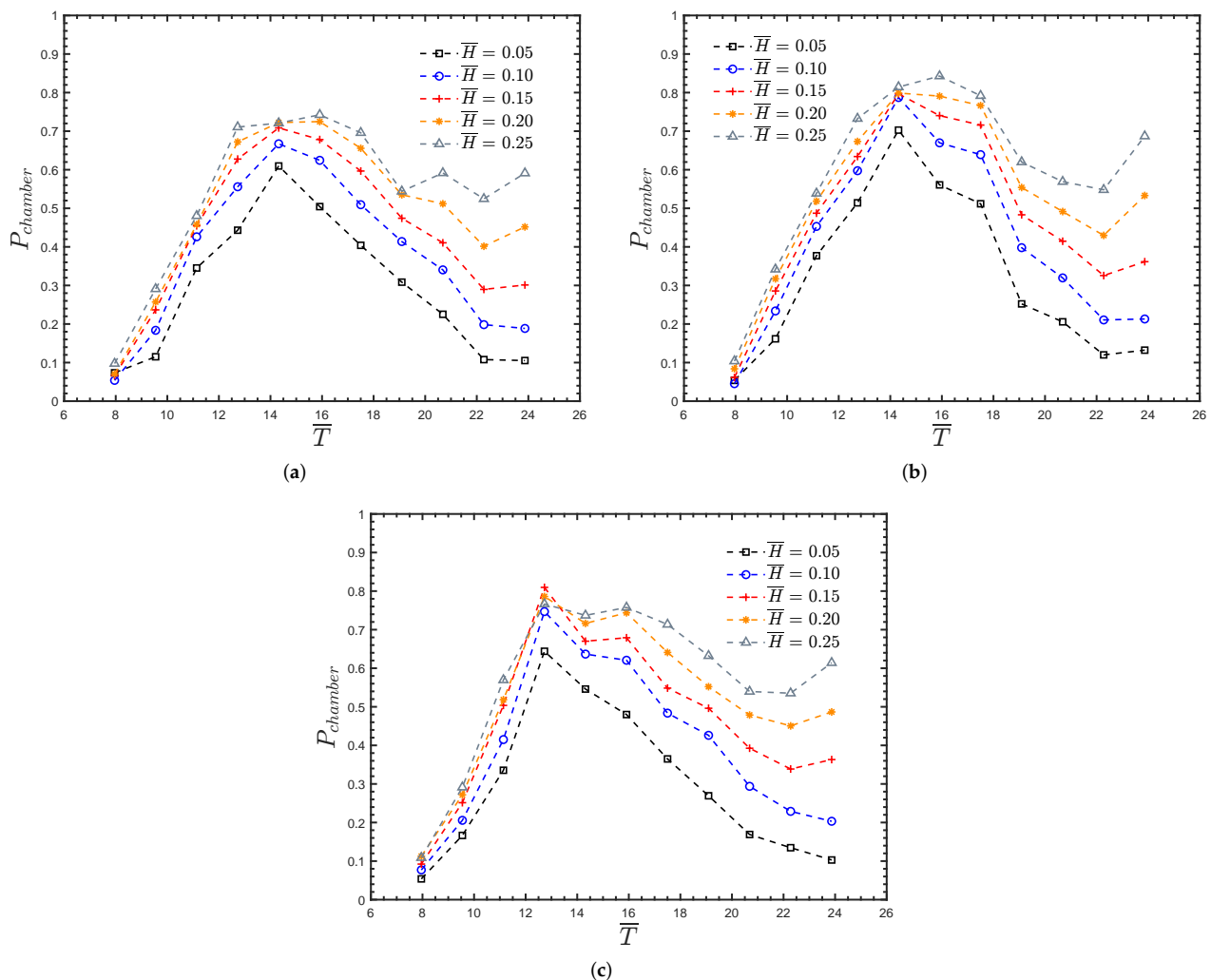


Figure 6. Non-dimensional air pressure versus \bar{T} for the nearshore OWC model. (a) Non-dimensional air pressure versus \bar{T} with $\theta = 0^\circ$ for the nearshore OWC model. (b) Non-dimensional air pressure versus \bar{T} with $\theta = 15^\circ$ for the nearshore OWC model. (c) Non-dimensional air pressure versus \bar{T} with $\theta = 30^\circ$ for the nearshore OWC model.

4.1.4. Phase Difference

In order to examine the effect of the wave period on the OWC performance, the time series quantifying the phase difference between α , $P_{chamber}$ and \bar{Q} versus t/T are shown in Figure 7a–f with $\theta = 0^\circ$ and $\theta = 30^\circ$. In Figure 7a,b it is observed that α and \bar{Q} are similar in amplitude and have a $\pi/2$ phase difference where the zero up and down-crossings in α correspond to the maximums and minimums in \bar{Q} , respectively. This can be directly inferred from Equation (10), since the volume flow rate is obtained with the time derivative of the free surface amplitude inside the chamber. Moreover, it is seen that the time series of the air pressure generated inside the chamber has the same frequency. However, comparing $P_{chamber}$ and \bar{Q} , it is observed that the amplitude in $P_{chamber}$ is small compared to that in \bar{Q} and a small phase difference between these exists. In this case, their amplitude and phase differences are very important, since in the hydrodynamic efficiency ε , P_{out} is calculated with the aid of Equation (9), where the output power of the system is the instantaneous integration of the product between the air pressure and volume flow rate, which infers that the smaller their product and the bigger the phase difference, the lower the efficiency. This explains the drop in OWC efficiency for wave periods shorter than the resonance period. In Figure 7c,d, the phase difference between α , $P_{chamber}$ and \bar{Q} is now shown at the corresponding resonant periods, i.e., $T = 1.8$ s for $\theta = 0^\circ$ and $T = 1.6$ s for $\theta = 30^\circ$. Here, it is observed that $P_{chamber}$ and \bar{Q} are better synchronized and the ratio of amplitudes between \bar{Q} and $P_{chamber}$ decreases, resulting in higher hydrodynamic efficiency as shown in Figure 5a–c. Finally, Figure 7e,f show the phase difference between α , $P_{chamber}$ and \bar{Q} for a long period ($T = 2.6$ s) which is beyond the resonant period of the device. This time a larger difference is seen between the bandwidth of the crests and troughs in \bar{Q} , while the maximums and minimums are below those observed in α . The $P_{chamber}$ and \bar{Q} values seem to be in phase, the amplitude of $P_{chamber}$ is seen to be higher than that recorded for $T = 1.0$ s, but is small compared to that of the resonant period, Figure 7c,d. Therefore, this leads to a decrease in the average power absorbed from regular waves and explains the reason behind the reduction in the hydrodynamic efficiency for long wavelengths.

4.2. Onshore OWC Model

In this subsection, the experimental results of the onshore OWC model (Figure 1b) are shown. Similar to the nearshore model, the wave amplification factor, hydrodynamic efficiency and air pressure inside the thick-front wall OWC chamber for different wave heights and incidence wave angles are presented and discussed. Additional findings for the pressure exerted on the walls of the onshore OWC model are presented in Appendix B.

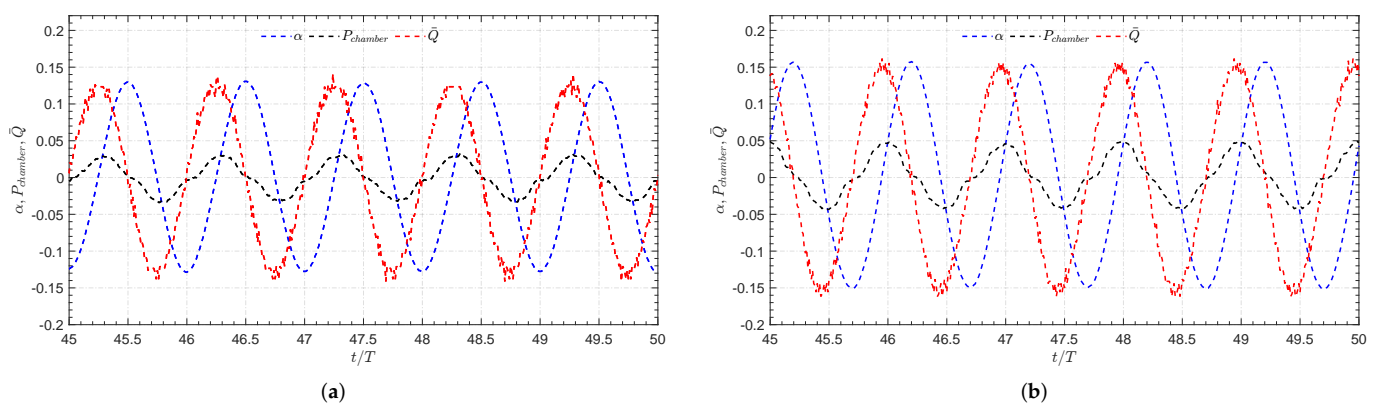


Figure 7. Cont.

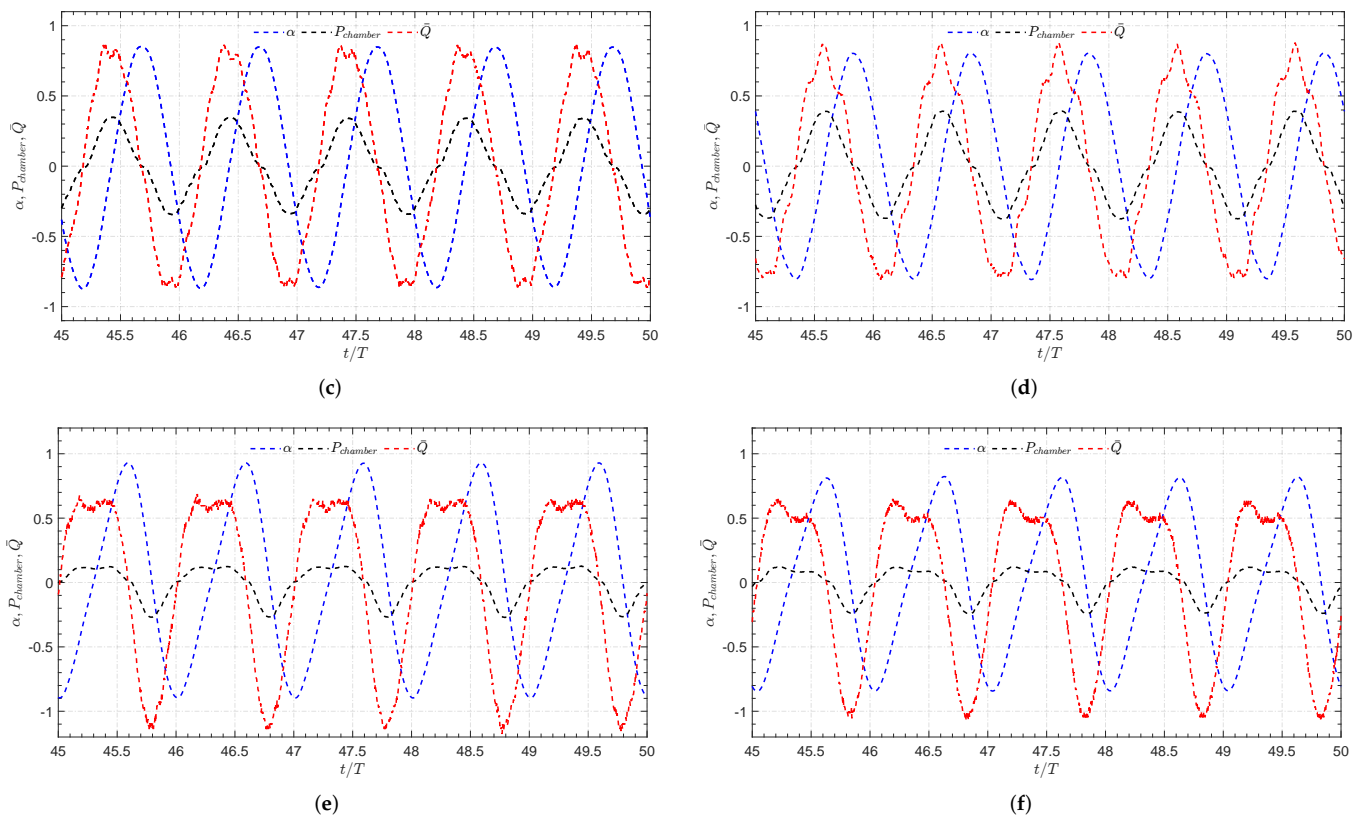


Figure 7. Phase difference between α , $P_{chamber}$ and \bar{Q} versus t/T for the nearshore OWC model. (a) Time series of α , $P_{chamber}$ and \bar{Q} with $\bar{H} = 0.15$, $\theta = 0^\circ$ and $\bar{T} = 7.96$ ($T = 1.0$ s). (b) Time series of α , $P_{chamber}$ and \bar{Q} with $\bar{H} = 0.15$, $\theta = 30^\circ$ and $\bar{T} = 7.96$ ($T = 1.0$ s). (c) Time series of α , $P_{chamber}$ and \bar{Q} with $\bar{H} = 0.15$, $\theta = 0^\circ$ and $\bar{T} = 14.32$ ($T = 1.8$ s). (d) Time series of α , $P_{chamber}$ and \bar{Q} with $\bar{H} = 0.15$, $\theta = 30^\circ$ and $\bar{T} = 12.73$ ($T = 1.6$ s). (e) Time series of α , $P_{chamber}$ and \bar{Q} with $\bar{H} = 0.15$, $\theta = 0^\circ$ and $\bar{T} = 20.68$ ($T = 2.6$ s). (f) Time series of α , $P_{chamber}$ and \bar{Q} with $\bar{H} = 0.15$, $\theta = 30^\circ$ and $\bar{T} = 20.68$ ($T = 2.6$ s).

4.2.1. Amplification Factor

Figure 8a,b show the wave amplification factor, α versus \bar{T} , inside the chamber for various non-dimensional wave heights \bar{H} and with $\theta = 0^\circ$ and 15° , respectively, for the onshore OWC model. In both figures, it is observed that the magnitude of the peak values is similar regardless of the wave direction. It is also seen that the wave amplification factor increases as the non-dimensional wave height \bar{H} decreases and that for the longest wave periods this non-dimensional parameter does not have a significant influence. The peak values in Figure 8a are around $17.50 < \bar{T} < 19.09$, while for Figure 8b are $15.91 < \bar{T} < 19.09$, i.e., the largest amplification inside the chamber is found when the OWC chamber interacts with waves long enough to transmit their energy below the thick wall into the chamber. Comparing the peaks in the wave amplification curves, there is an increase of almost 60% between $H = 0.05$ and $H = 0.25$. Furthermore, comparing Figures 8a and 4a for $\theta = 0^\circ$, it is observed that for the onshore OWC model the maximum wave amplification is higher and occurs for longer periods. This increase in the wave amplification is due to the interaction between the incident waves and those reflected by the artificial beach. A comparison of Figures 4a,b and 8a,b for $\theta = 0^\circ$ and 15° shows that the curve bandwidth is not significantly affected by the location of the OWC model.

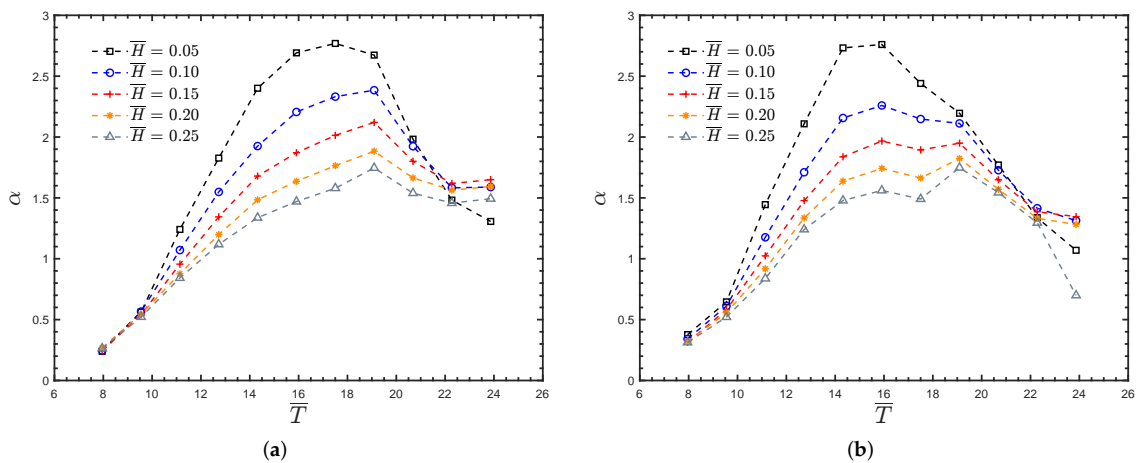


Figure 8. Variation of amplification factor α versus \bar{T} for the onshore OWC model. (a) Amplification factor α versus \bar{T} with $\theta = 0^\circ$ for the onshore OWC model. (b) Amplification factor α versus \bar{T} with $\theta = 15^\circ$ for the onshore OWC model.

4.2.2. Hydrodynamic Efficiency

The hydrodynamic efficiency ϵ versus the non-dimensional wave period \bar{T} for two incident wave angles $\theta = 0^\circ$ and 15° and various non-dimensional wave heights \bar{H} is shown in Figure 9a,b. As in the nearshore OWC model, it is observed that for short and long wave periods, ϵ increases when \bar{H} increases. However, for periods close to the resonance condition, the hydrodynamic efficiency decreases when \bar{H} increases. As a result, we see that regardless of whether it is a nearshore or onshore device, wave height can play an important role in the hydrodynamic performance of a land fixed OWC device. In Figures 5a,b and 9a,b, it is observed that the magnitude of the hydrodynamic efficiency is not significantly influenced by the location of the OWC model, while the value of the non-dimensional wave period at which resonance occurs remains unaltered. Comparing Figures 5a and 9a, it is seen that the average value of the efficiency at resonance is around 4% more for the nearshore OWC model. However, comparing Figures 5b and 9b, where an incident wave direction of $\theta = 15^\circ$ was considered, it was found that the value of the efficiency at resonance is between 5% and 13% more for the onshore OWC device than for the nearshore OWC model, which is may be due to the constructive interference between the incident and reflected waves by the artificial beach.

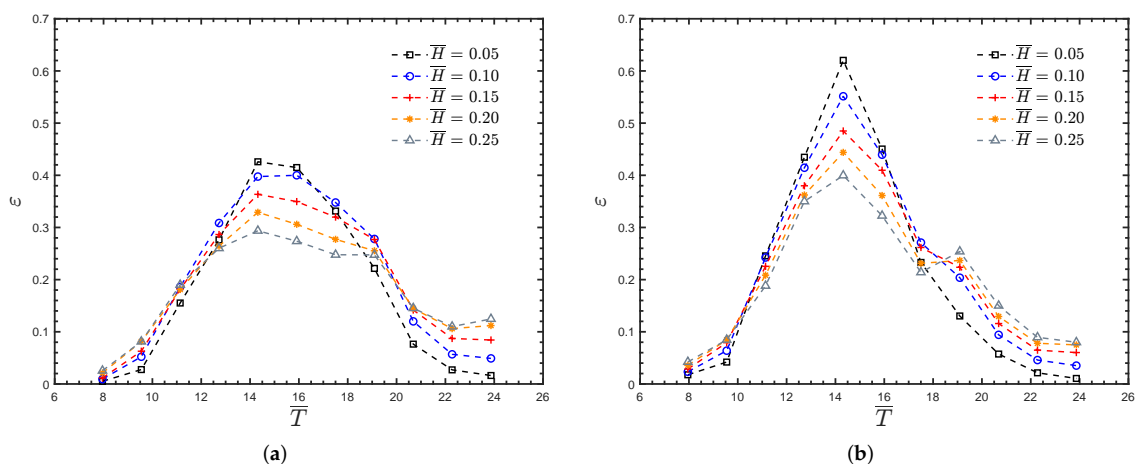


Figure 9. Hydrodynamic efficiency ϵ versus \bar{T} for the onshore OWC model. (a) Hydrodynamic efficiency ϵ versus \bar{T} with $\theta = 0^\circ$ for the onshore OWC model. (b) Hydrodynamic efficiency ϵ versus \bar{T} with $\theta = 15^\circ$ for the onshore OWC model.

4.2.3. Non-Dimensional Air Pressure

Figures 10a,b show the dimensionless air pressure inside the OWC chamber $P_{chamber}$ versus \bar{T} for various non-dimensional wave heights \bar{H} and wave direction $\theta = 0^\circ$ and 15° . Similar to the previous results for the nearshore OWC model, these figures show that the maximum values in $P_{chamber}$ occur close to the resonance period of the chamber ($T = 1.8$ s) and that the magnitudes and trends of the curves are similar, with a slight increase in $P_{chamber}$ of the onshore model for medium and high non-dimensional wave periods. Again, it is seen that as the wave height parameter increases, the dimensionless air pressure within the chamber also increases, although the increase is more significant between the small dimensionless wave heights \bar{H} . The results therefore demonstrate two things, that the artificial beach near the land-fixed OWC device does not significantly alter the air pressure within the chamber and that the combination of higher wave heights with longer wavelengths can contribute to increasing the air pressure. Comparing Figure 10b and Figure 10a, it is observed that for $\theta = 15^\circ$, the maximum values of $P_{chamber}$ are an average 8% more than those obtained for $\theta = 0^\circ$.

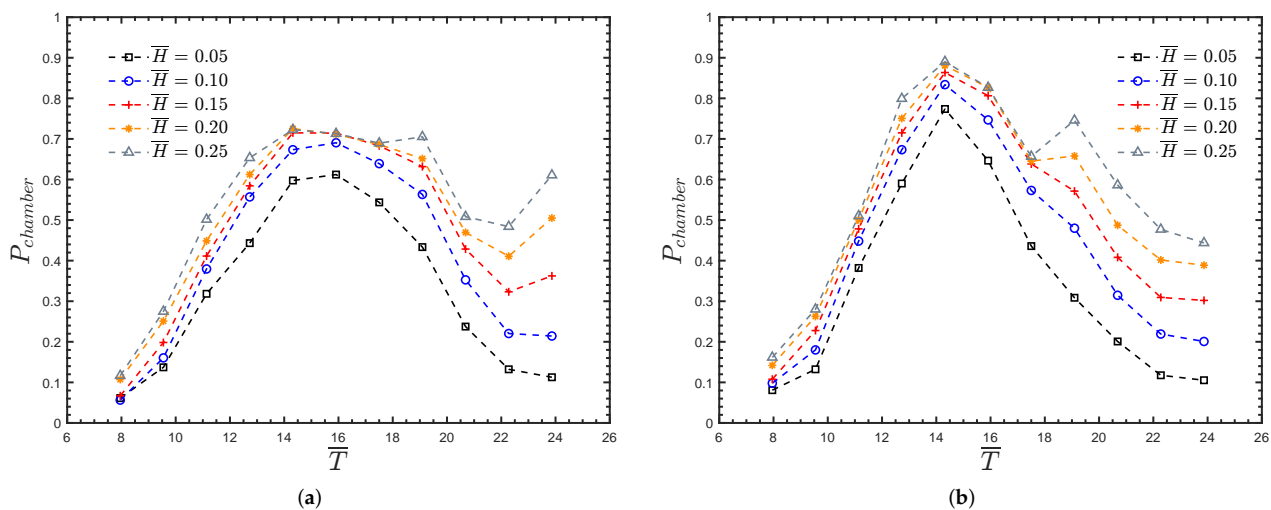


Figure 10. Non-dimensional air pressures versus \bar{T} for the onshore OWC model. (a) Non-dimensional air pressure versus \bar{T} with $\theta = 0^\circ$ for the onshore OWC model. (b) Non-dimensional air pressure versus \bar{T} with $\theta = 15^\circ$ for the onshore OWC model.

4.2.4. Phase Difference

The time series quantifying the phase difference between α , $P_{chamber}$ and \bar{Q} versus t/T with $\theta = 0^\circ$ and $\theta = 15^\circ$ for the onshore OWC device are shown in Figure 11a–f. As for the nearshore device, for $T = 1.0$ s, in Figure 11a,b, it is seen that α and \bar{Q} have a phase difference $\pi/2$, the amplitudes of α and \bar{Q} are similar, while the amplitude in $P_{chamber}$ is small. This phase difference and low amplitude in \bar{Q} result in low hydrodynamic efficiency for short periods. In Figure 11c,d, the dimensionless time series of α , $P_{chamber}$ and \bar{Q} are shown at the resonant period $T = 1.8$ s. Here, regardless of the wave angle, it is observed that $P_{chamber}$ and \bar{Q} are in phase in both cases, their amplitudes increase, giving the maximum values of hydrodynamic efficiency ε , shown in Figure 9a,b. Finally, Figure 11e,f show the dimensionless time series of α , $P_{chamber}$ and \bar{Q} for the same long period ($T = 2.6$ s), which is beyond the resonant period of the device. Here, the difference between the bandwidth of the crests and troughs in \bar{Q} is evident, the phase difference between $P_{chamber}$ and \bar{Q} is almost insignificant but the amplitude of $P_{chamber}$ decreases compared to that observed for the resonant period, Figure 11c,d, thereby giving in a reduction in the hydrodynamic efficiency.

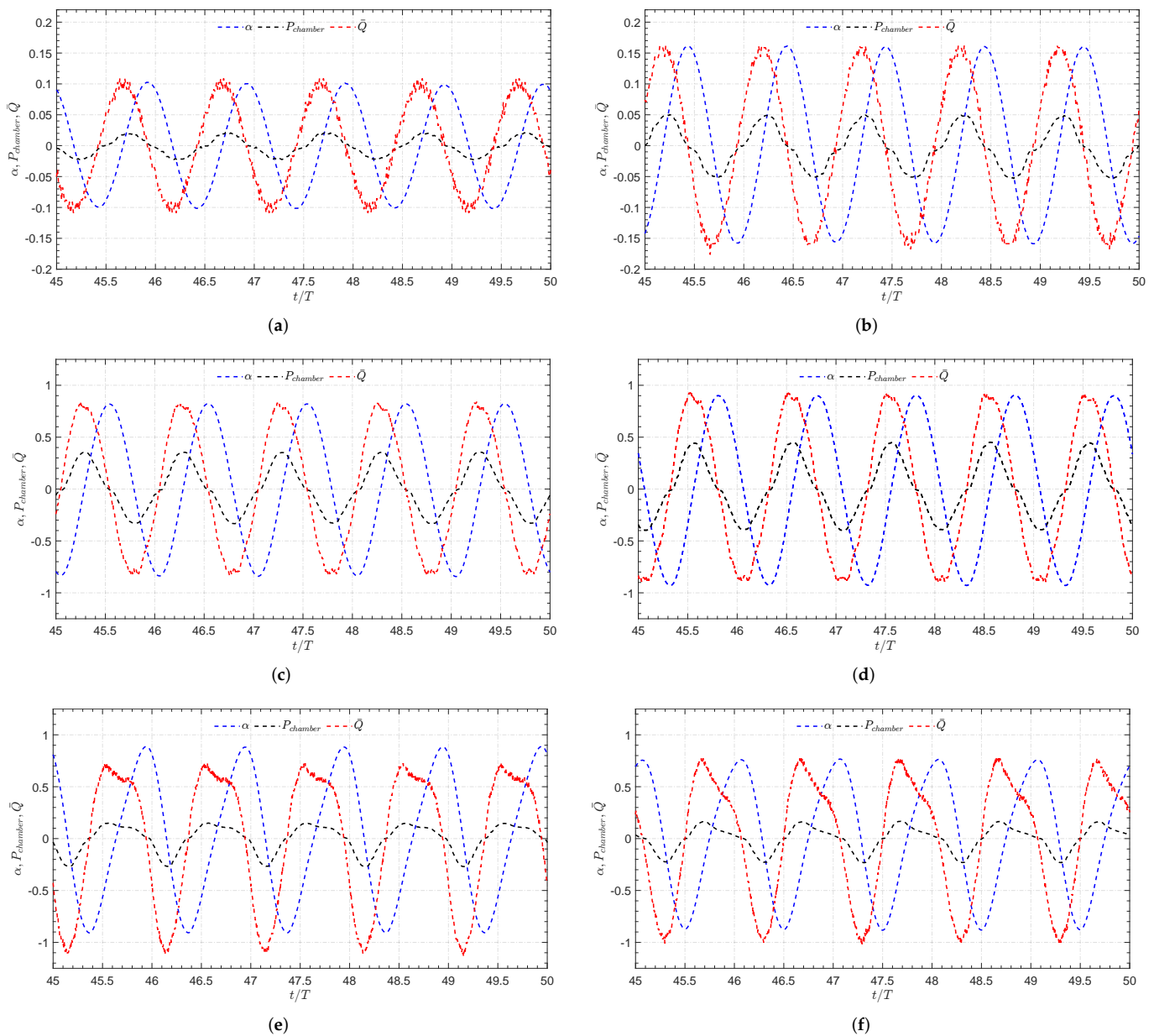


Figure 11. Phase difference between α , $P_{chamber}$ and \bar{Q} versus t/T for the onshore OWC model. (a) Time series of α , $P_{chamber}$ and \bar{Q} with $\bar{H} = 0.15$, $\theta = 0^\circ$ and $\bar{T} = 7.96$ ($T = 1.0$ s). (b) Time series of α , $P_{chamber}$ and \bar{Q} with $\bar{H} = 0.15$, $\theta = 15^\circ$ and $\bar{T} = 7.96$ ($T = 1.0$ s). (c) Time series of α , $P_{chamber}$ and \bar{Q} with $\bar{H} = 0.15$, $\theta = 0^\circ$ and $\bar{T} = 14.32$ ($T = 1.8$ s). (d) Time series of α , $P_{chamber}$ and \bar{Q} with $\bar{H} = 0.15$, $\theta = 15^\circ$ and $\bar{T} = 14.32$ ($T = 1.8$ s). (e) Time series of α , $P_{chamber}$ and \bar{Q} with $\bar{H} = 0.15$, $\theta = 0^\circ$ and $\bar{T} = 20.68$ ($T = 2.6$ s). (f) Time series of α , $P_{chamber}$ and \bar{Q} with $\bar{H} = 0.15$, $\theta = 15^\circ$ and $\bar{T} = 20.68$ ($T = 2.6$ s).

5. Conclusions

The effects of wave angle of incidence and wave height on the hydrodynamic performance on nearshore and onshore land-fixed, thick front wall OWC devices under regular waves were assessed. Based on the results of the experimental tests, the following conclusions may be drawn. Wave height has a significant influence on the performance of the nearshore and onshore OWC devices. For short and long wave periods, the hydrodynamic efficiency and the bandwidth of the curves increase when wave height increases. The exception is at the resonance period, where the lower the incident wave height, the greater the hydrodynamic efficiency. A similar pattern of results was obtained in [25] for an OWC

model under regular waves with a high turbine damping condition. However, in the two configurations of the OWC device examined, the results demonstrate that the height of the incoming wave does not affect the periods at which resonance occurs. Regarding the wave direction, it was observed that for the nearshore OWC device where three different wave directions were presented, the period at which resonance occurs is lower when the incident wave angle is higher. A different conclusion was reached by Ashlin et al. [24], who investigated an array of OWCs integrated into an offshore detached breakwater. They found that the natural frequency of the system remains unaltered for the incident wave angles studied ($\theta = 0^\circ, 10^\circ$ and 20°).

Our results demonstrate that not only the phase difference between the dimensionless volumetric flow rate and the air pressure play important roles in the hydrodynamic efficiency, but also the amplitude of the air pressure within the chamber. It was observed that at the resonance period, these two aspects were in phase, and their magnitudes were relatively large; for short and long periods, a small phase difference was observed and the amplitude of the pressure within the chamber was small. Compared to the wave amplification, the peaks in hydrodynamic efficiency occur for shorter wave periods and, in fact, these resonance periods in the hydrodynamic efficiency are associated with those observed for the average air pressure inside the chamber.

Furthermore, for both the nearshore and onshore OWC models, the wave amplification factor was found to increase as the wave height decreases. As explained above, the maximum amplification was reached for greater periods than that at the resonance of the chamber, indicating that energy transmission is improved when longer waves interact with the thick front wall of the OWC device. From the results, it is clear that the wave angle of incidence and the location of the OWC device does not significantly affect the amplification factor. When steep waves interact with the OWC chamber, a reduction in the water surface oscillation, efficiency and pressure inside the chamber was seen. This is explained by the higher energy dissipation, due to turbulence, vortex shedding, etc., at the bottom part of the front wall. The non-dimensional pressures in the bottom and the interior face of the front wall and in the back wall were found to increase when wave height decreased for intermediate and long wave periods. Similar trends amongst these processes are seen, and the value of the wave period at which the peak values occur is linked to the maximum wave amplification within the OWC chamber.

Finally, it is hoped that the findings of this study motivate further research into the effect of wave direction on the performance of land-based OWC nearshore and onshore devices, as well as giving helpful information for the effective extraction of ocean wave energy.

Author Contributions: Conceptualization, A.A.M.R., G.P.V., R.S.C., E.G.M.B., B.E.V.S., F.E.P.C. and E.A.M.C.; methodology, A.A.M.R., G.P.V., R.S.C., E.G.M.B., B.E.V.S., F.E.P.C. and E.A.M.C.; software, A.A.M.R., G.P.V., R.S.C., E.G.M.B., B.E.V.S., F.E.P.C. and E.A.M.C.; validation, A.A.M.R., G.P.V., R.S.C., E.G.M.B., B.E.V.S., F.E.P.C. and E.A.M.C.; formal analysis, A.A.M.R., G.P.V., R.S.C., E.G.M.B., B.E.V.S., F.E.P.C. and E.A.M.C.; investigation, A.A.M.R., G.P.V., R.S.C., E.G.M.B., B.E.V.S., F.E.P.C. and E.A.M.C.; data curation, A.A.M.R., G.P.V., R.S.C., E.G.M.B., B.E.V.S., F.E.P.C. and E.A.M.C.; writing—original draft preparation, A.A.M.R., G.P.V., R.S.C., E.G.M.B., B.E.V.S., F.E.P.C. and E.A.M.C.; writing—review and editing, A.A.M.R., G.P.V., R.S.C., E.G.M.B., B.E.V.S., F.E.P.C. and E.A.M.C.; visualization, A.A.M.R., G.P.V., R.S.C., E.G.M.B., B.E.V.S., F.E.P.C. and E.A.M.C.; supervision, G.P.V., R.S.C., E.G.M.B., B.E.V.S.; funding acquisition, G.P.V., R.S.C., E.G.M.B. and B.E.V.S. All authors have read and agreed to the published version of the manuscript.

Funding: This study was developed under the framework of CEMIE-Océano (Mexican Centre for Innovation in Ocean Energy). Project FSE-2014-06-249795 financed by CONACYT-SENER- Sustentabilidad Energética. G. Posada Vanegas also wants to thank VTI-Spain for the support provided for the tuning of the wave tank.

Institutional Review Board Statement: Not applicable.

Informed Consent Statement: Not applicable.

Data Availability Statement: Not applicable.

Conflicts of Interest: The authors declare no conflict of interest.

Appendix A. Water Pressure for the Nearshore OWC Device

Appendix A.1. Non-Dimensional Pressures for $\theta = 0^\circ$

Figure A1a–d show the non-dimensional water pressures on: the sea side P_{fwout} , the bottom of the front wall $P_{fwbottom}$, on the lee-side of the front wall P_{fwin} and on the bottom of the back wall P_{bw} , respectively, versus the non-dimensional wave period \bar{T} for various non-dimensional wave heights \bar{H} and $\theta = 0^\circ$. The measurements are based on Equation (11a–d), where the difference between the maximum and minimum values of the pressures was used for the calculation. Figure A1a shows that the variation of the non-dimensional pressure P_{fwout} is reduced as the dimensionless wave height increases. In the case of $P_{fwbottom}$, Figure A1b shows that the dimensionless pressure at the lower part of the front wall increases when \bar{H} increases for intermediate values of the wave period, while for long and short wave periods the trend was the opposite. This is a similar trend to that seen in hydrodynamic efficiency, Figure 5a. It is also observed that the magnitude of P_{fwout} , where these peak values occur in $P_{fwbottom}$, is close to that observed in the amplification factor, Figure 4a. This is because close to the values of dimensionless wave period, where there is maximum amplification of the free surface elevation, the waves that interact with the OWC device are less steep, and the vortex sheddings at the tip of the front wall are reduced, thus increasing the pressure. In Figure A1c, it is observed that P_{fwin} increases for a wide range of \bar{T} when the dimensionless wave height \bar{H} decreases, while for long wave periods, the pressure is small and hardly varies with \bar{H} . This again is explained by the fact that when steeper waves interact with the OWC chamber, the energy dissipation (due to turbulence, vortex shedding, etc.) at the gap below the front wall is higher, compared to that created by less steep waves. This leads to higher energy loss, decreasing water surface oscillation and thus the pressure inside the chamber [27,47]. On the other hand, as with $P_{fwbottom}$ and P_{fwin} , Figure A1d shows that the dimensionless pressure at the lower part of the back wall increases when \bar{H} increases, except for long and short wave periods. It is also observed that for the values of \bar{T} where the peaks occur, the trends and shapes of the curves are similar to those obtained for P_{fwin} , these two being measured inside the OWC chamber.

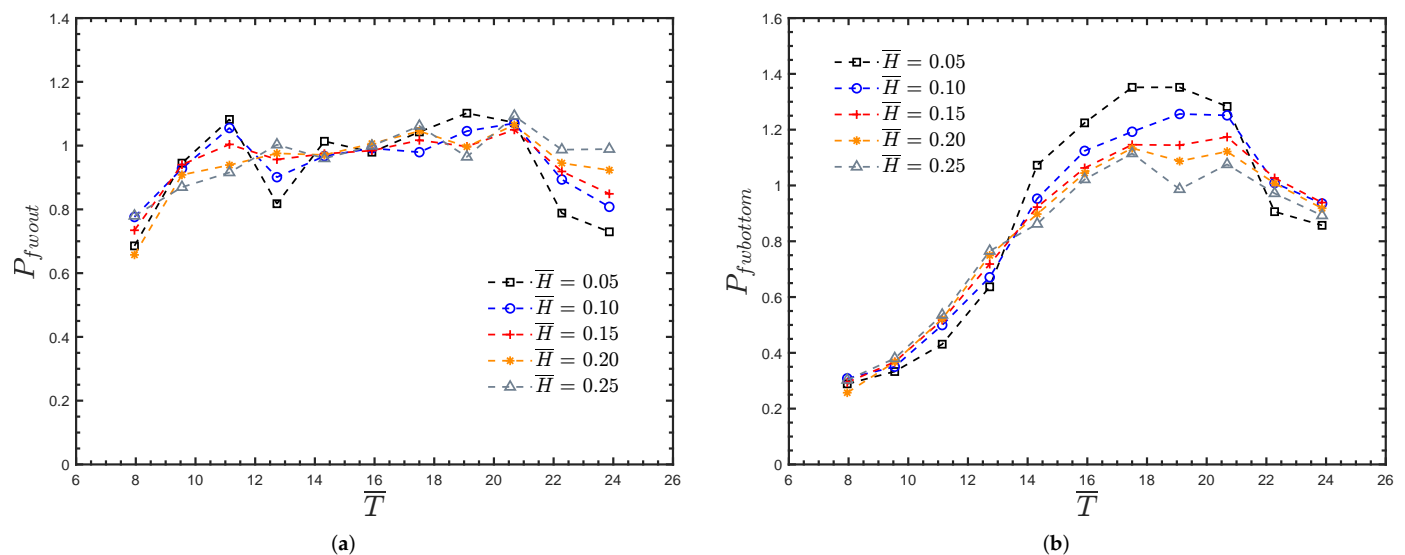


Figure A1. Cont.

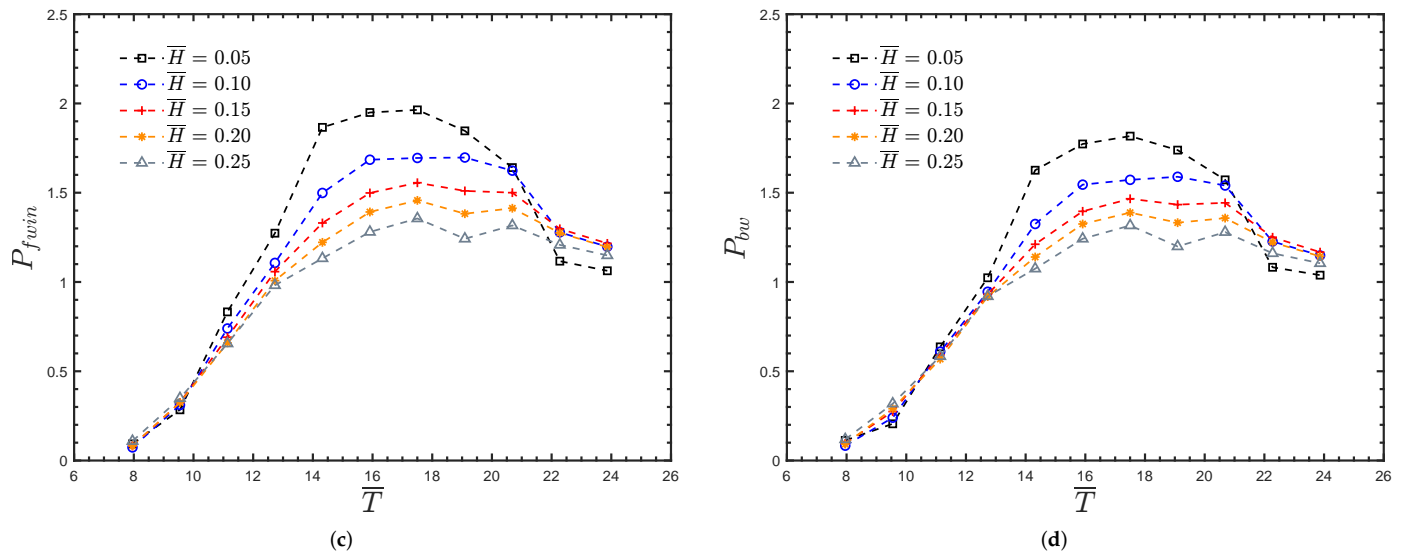


Figure A1. Non-dimensional pressures versus \bar{T} with $\theta = 0^\circ$ for the nearshore OWC model. (a) Non-dimensional pressure outside the front wall P_{fwout} versus \bar{T} . (b) Non-dimensional pressure at the bottom tip of the front wall $P_{fwbottom}$ versus \bar{T} . (c) Non-dimensional pressure inside the front wall P_{fwin} versus \bar{T} . (d) Non-dimensional pressure at the bottom of the back wall P_{bw} versus \bar{T} .

Appendix A.2. Non-Dimensional Pressures for $\theta = 15^\circ$

Figure A2a–d show the non-dimensional water pressures P_{fwout} , $P_{fwbottom}$, P_{fwin} and P_{bw} , respectively, versus the non-dimensional wave period, \bar{T} , for different non-dimensional wave heights \bar{H} and $\theta = 15^\circ$. Figure A2a shows that P_{fwout} increases when the dimensionless wave height \bar{H} increases for long wave periods. It is also observed that the minimum value of the curves for small \bar{H} occurs at $\bar{T} = 22.28$ and 12.73 . The latter is related to the resonant period observed in the hydrodynamic efficiency ε , Figure 5b. Furthermore, compared to the case when $\theta = 0^\circ$, the magnitude of the non-dimensional pressure P_{fwout} increases, especially for long periods. In Figure A2b an increase in $P_{fwbottom}$ is seen when longer and shorter waves interact with the OWC chamber. Furthermore, the maximum amplification inside the chamber, observed in Figure 4b, is related to the maximum pressure below the front wall since these maximums occur in the same wave period. On the other hand, the difference between the peaks in $\bar{H} = 0.05$ and 0.25 is approximately 30%, and is attributed to the lower energy loss when less steep waves interact with the front wall. Figure A2c shows that, as in the case of normal incidence, P_{fwin} increases when \bar{H} increases, and the magnitude of the peaks in P_{fwin} at $\bar{T} = 17.50$ are an average 15% more than those obtained for $\theta = 0^\circ$, see Figure A1c. In Figure A2d again it is seen that the effect of steeper waves on the pressure; an increase in the non-dimensional wave height \bar{H} leads to a decrease in the non-dimensional pressure P_{bw} when long waves interact with the OWC chamber. As in Figures 4b and A2b,c, the peaks in the dimensionless pressure P_{bw} occur at $\bar{T} = 17.50$.

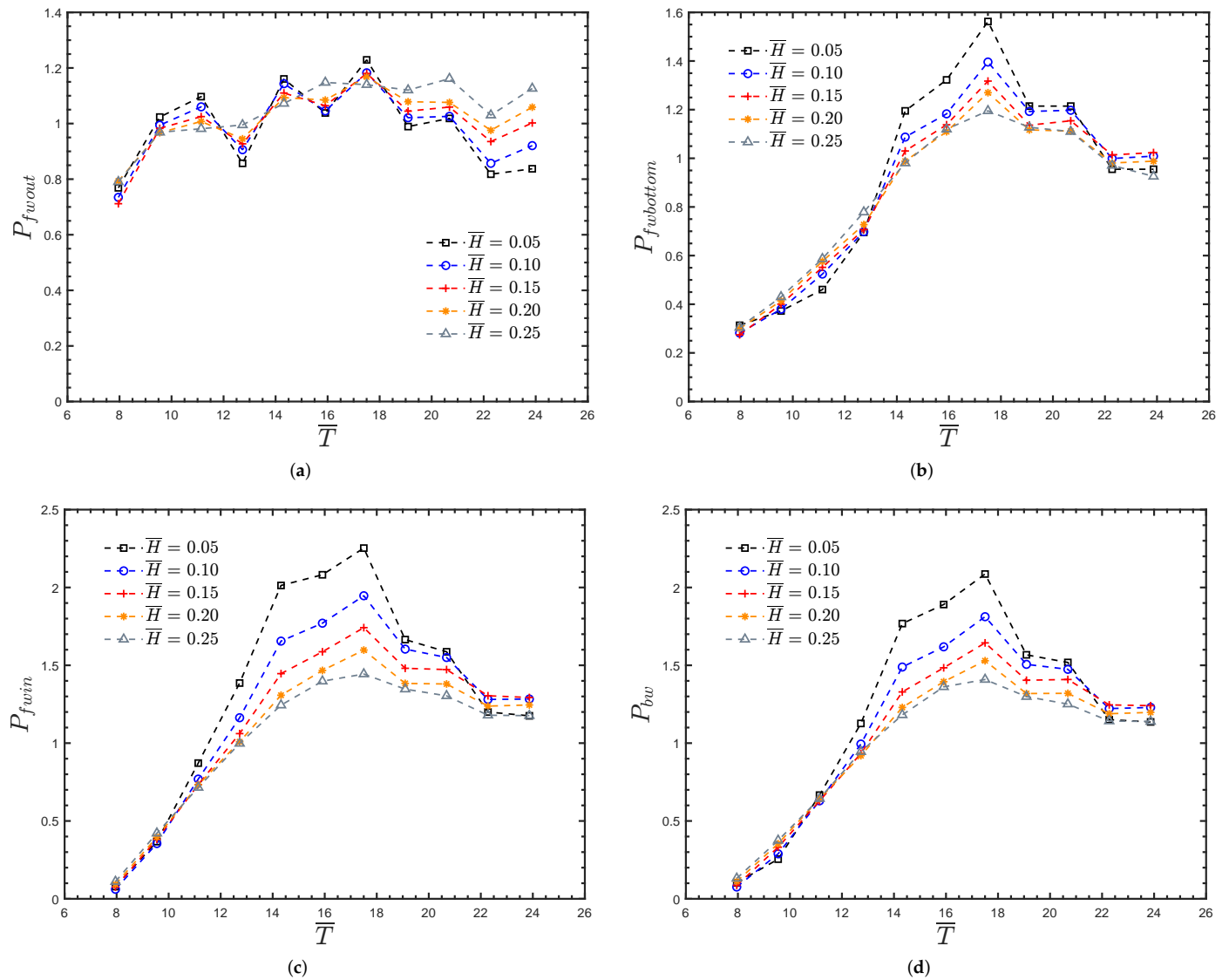


Figure A2. Non-dimensional pressures versus \bar{T} with $\theta = 15^\circ$ for the nearshore OWC model. (a) Non-dimensional pressure outside the front wall P_{fwout} versus \bar{T} . (b) Non-dimensional pressure at the bottom tip of the front wall $P_{fwbottom}$ versus \bar{T} . (c) Non-dimensional pressure inside the front wall P_{fwin} versus \bar{T} . (d) Non-dimensional pressure at the bottom of the back wall P_{bw} versus \bar{T} .

Appendix A.3. Non-Dimensional Pressures for $\theta = 30^\circ$

The non-dimensional water pressures P_{fwout} , $P_{fwbottom}$, P_{fwin} and P_{bw} are shown, respectively, in Figure A3a–d versus the non-dimensional wave period \bar{T} for different non-dimensional wave heights \bar{H} and $\theta = 30^\circ$. Unlike the two previous wave angles, this figure shows a maximum value at $\bar{T} \approx 12.73$, which corresponds to the natural period of the OWC model of 1.6 s. This maximum pressure is due to wave amplification in front of the chamber and higher reflection. In general, it is seen that the dimensionless parameter \bar{H} has a significant influence on P_{fwout} , up to 10% for low-frequency waves. In Figure A3b it is seen that $P_{fwbottom}$ increases with a decrease in \bar{H} for $\bar{T} > 12.73$. However, for short wavelengths, $P_{fwbottom}$ increases when \bar{H} increases. Compared to Figure A2b, the magnitude of the peak values is reduced by approximately 10%. On the other hand, similar to the cases when $\theta = 0^\circ$ and 15° , P_{fwin} exhibits a similar increasing trend, with an increase in \bar{T} and then a reduction for long wave periods. Furthermore, the bandwidth is wider in the P_{fwin} curves when the dimensional wave height \bar{H} decreases, and at $\bar{T} < 11$,

i.e., small wavelengths, the pressure does not vary significantly with a modification in \bar{H} . In Figure A3d it is observed that P_{bw} increases when the non-dimensional wave period increases. This is because energy transmission is improved when larger waves interact with the thick front wall of the OWC device, thus increasing the pressure inside the chamber.

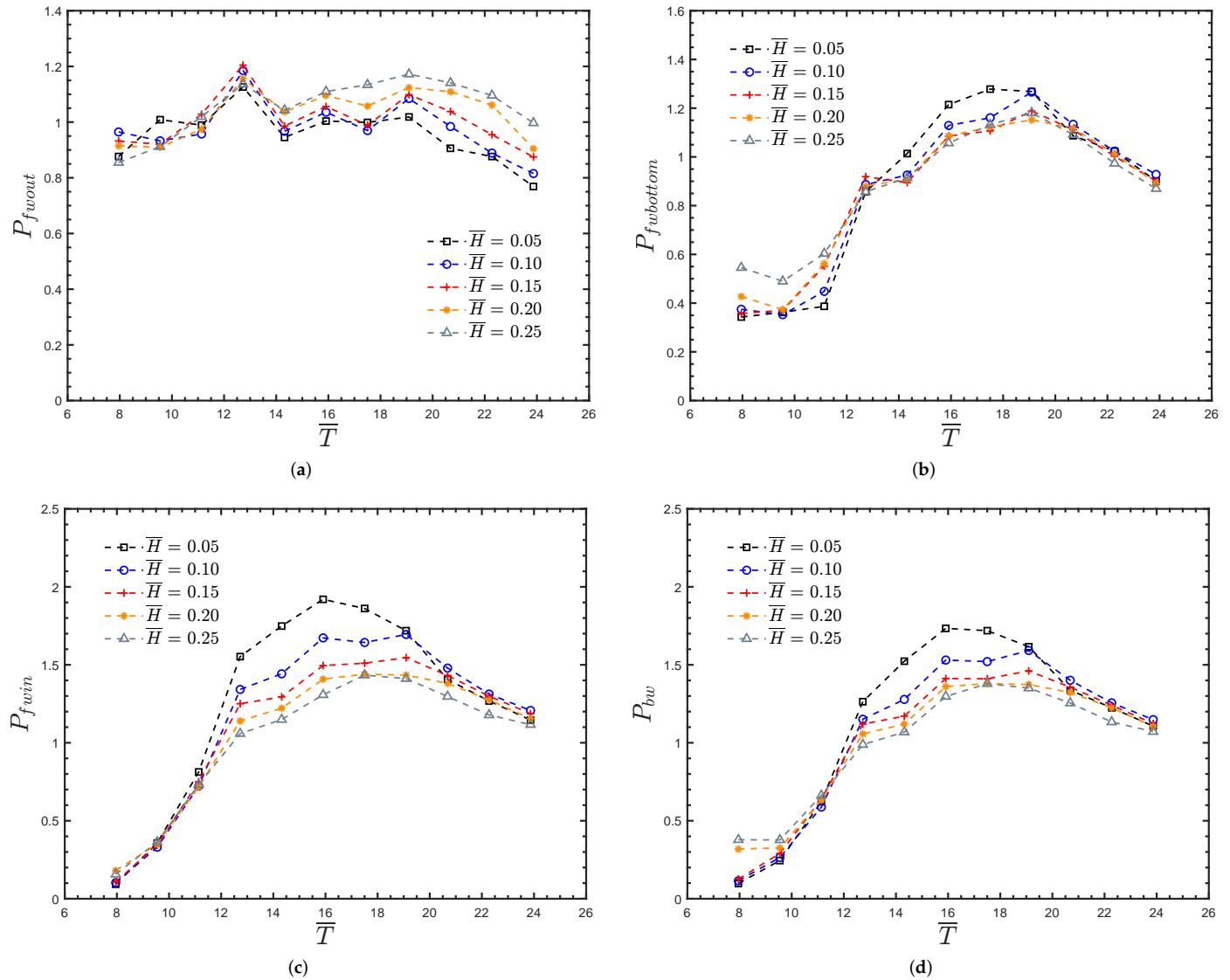


Figure A3. Non-dimensional pressures versus \bar{T} with $\theta = 30^\circ$ for the nearshore OWC model. (a) Non-dimensional pressure outside the front wall P_{fwout} versus \bar{T} . (b) Non-dimensional pressure at the bottom tip of the front wall $P_{fwbottom}$ versus \bar{T} . (c) Non-dimensional pressure inside the front wall P_{fwin} versus \bar{T} . (d) Non-dimensional pressure at the bottom of the back wall P_{bw} versus \bar{T} .

Appendix B. Water Pressure for the Onshore OWC Device

Appendix B.1. Non-Dimensional Pressures for $\theta = 0^\circ$

For the onshore OWC model, Figure A4a–d show the dimensionless pressures P_{fwout} , $P_{fwbottom}$, P_{fwin} and P_{bw} , respectively, versus the non-dimensional wave period \bar{T} for different values of \bar{H} and $\theta = 0^\circ$. Figure A4a shows that the peak occurs at $\bar{T} = 19.09$, increasing when the non-dimensional wave height \bar{H} decreases, while the opposite is observed for $\bar{T} > 20.68$. In Figure A4b it is observed that for high frequencies, the pressure ratio $P_{fwbottom}$ increases when \bar{H} increases, while the opposite occurs for $\bar{T} > 12.73$, where the peaks in $P_{fwbottom}$ are higher when \bar{H} decreases. It is also seen that the peaks in $P_{fwbottom}$ and α ,

Figure 8b, occur at similar values of \bar{T} . Therefore, an increase in the amplification of the free surface elevation within the chamber is related to an increase in the pressure below the front wall. This occurs when fewer vortices develop near the lip wall and less radiated flow is generated inside the chamber. Figure A4c shows that the peaks in pressure on the interior face of the front wall occur at $\bar{T} = 19.09$. In these peaks, an increase of almost 50% is seen for $\bar{H} = 0.05$ with respect to $\bar{H} = 0.25$. Figure A4d shows that the pressure on the back wall increases when \bar{T} increases, but at $\bar{T} \leq 11.14$ the pressure remains almost unaltered by a modification in the non-dimensional wave height \bar{H} . Again, the peaks in P_{bw} occur at $\bar{T} = 19.09$.

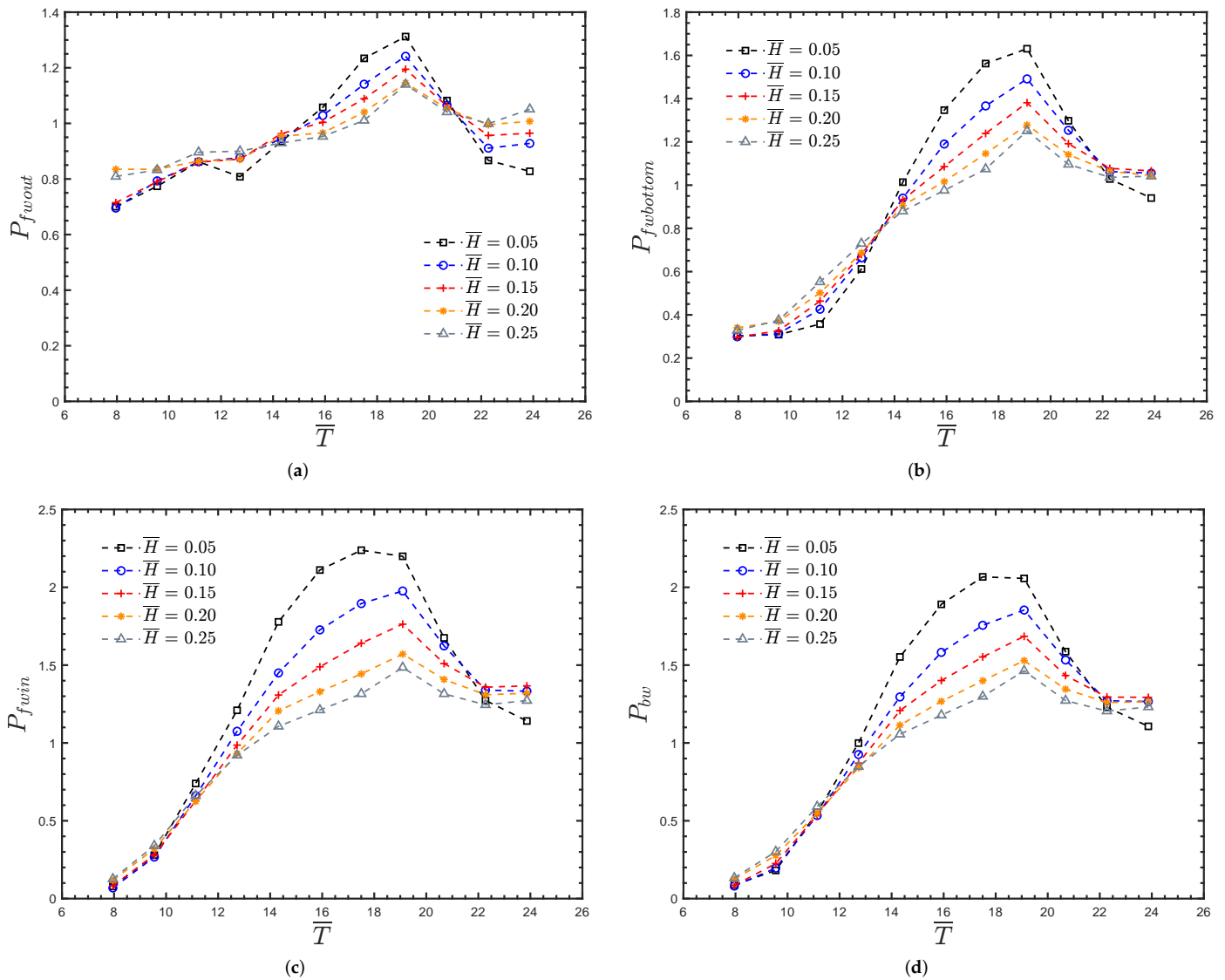


Figure A4. Non-dimensional pressures versus \bar{T} with $\theta = 0^\circ$ for the onshore OWC model. (a) Non-dimensional pressure outside the front wall P_{fwout} versus \bar{T} . (b) Non-dimensional pressure at the bottom tip of the front wall $P_{fwbottom}$ versus \bar{T} . (c) Non-dimensional pressure inside the front wall $P_{fwinside}$ versus \bar{T} . (d) Non-dimensional pressure at the bottom of the back wall P_{bw} versus \bar{T} .

Appendix B.2. Non-Dimensional Pressures for $\theta = 15^\circ$

The non-dimensional water pressures P_{fwout} , $P_{fwbottom}$, $P_{fwinside}$ and P_{bw} are shown, respectively, in Figure A5a–d versus the non-dimensional wave period \bar{T} for different non-dimensional wave heights \bar{H} and $\theta = 15^\circ$. In Figure A5a it is observed that P_{fwout} reaches a maximum for intermediate values of the non-dimensional wave period, while for

quite long wave periods P_{fwout} decreases. In general, it is seen that for an increase in the non-dimensional wave heights \bar{H} , the magnitude of P_{fwout} does not vary significantly. On the other hand, comparing the results in Figure A5b with those in Figure A4b, a reduction of $P_{fwbottom}$ at the peak values when $\bar{H} \geq 0.15$ is seen. Furthermore, as \bar{H} increases, it is seen that the peaks are more pronounced at $\bar{T} = 19.09$, which may be due to the interaction between the oblique incident waves and the waves reflected by the artificial beach. In Figure A5c it is seen that P_{fwin} increases as \bar{H} decreases for a wide range of \bar{T} . Comparing these results with those for $\theta = 0^\circ$, it is observed that the non-dimensional pressure P_{fwin} increases at intermediate values of the non-dimensional wave period \bar{T} . Finally, Figure A5d shows a similar trend to that observed in $P_{fwbottom}$ and P_{fwin} ; for short waves, the dimensionless pressure P_{bw} is not affected by the non-dimensional wave height \bar{H} , while for intermediate wave periods, the smaller the wave height, the higher the peak in P_{bw} .

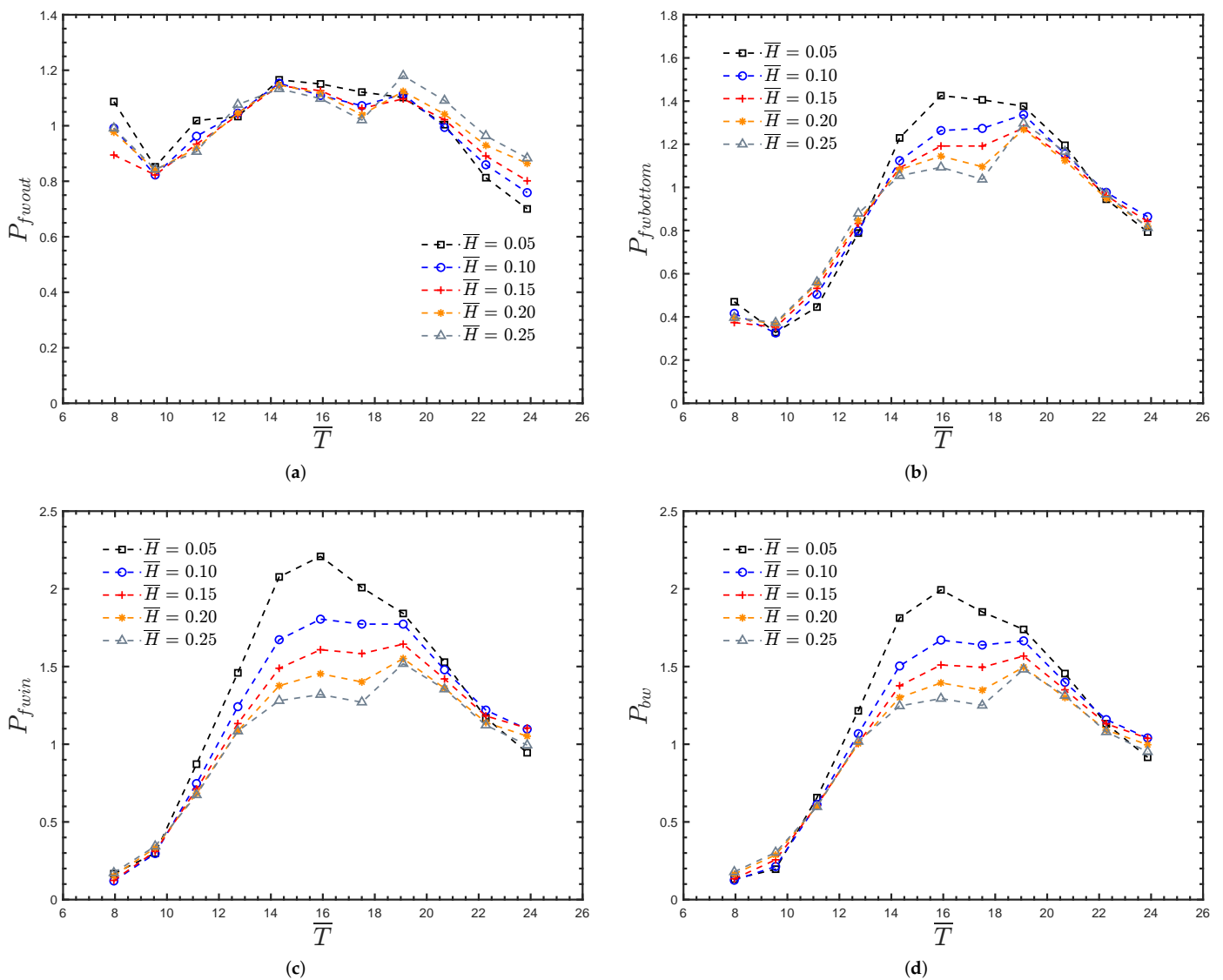


Figure A5. Non-dimensional pressures versus \bar{T} with $\theta = 15^\circ$ for the onshore OWC model. (a) Non-dimensional pressure outside the front wall P_{fwout} versus \bar{T} . (b) Non-dimensional pressure at the bottom tip of the front wall $P_{fwbottom}$ versus \bar{T} . (c) Non-dimensional pressure inside the front wall P_{fwin} versus \bar{T} . (d) Non-dimensional pressure at the bottom of the back wall P_{bw} versus \bar{T} .

References

1. REN21 Renewables Now. Available online: <https://www.ren21.net/> (accessed on 26 November 2021).
2. Hussain, A.; Arif, S.M.; Aslam, M. Emerging renewable and sustainable energy technologies: State of the art. *Renew. Sustain. Energy Rev.* **2017**, *71*, 12–28. [[CrossRef](#)]
3. Drew, B.; Plummer, A.R.; Sahinkaya, M.N. A review of wave energy converter technology. *Proc. Inst. Mech. Eng. Part A J. Power Energy.* **2009**, *223*, 887–902. [[CrossRef](#)]
4. Titah-Benbouzid, H.; Benbouzid, M. Ocean wave energy extraction: Up-to-date technologies review and evaluation. In Proceedings of the International Power Electronics and Application Conference and Exposition, Shanghai, China, 5–8 November 2014; pp. 338–342.
5. McCormick, M. *Ocean Wave Energy Conversion*; Dover Civil and Mechanical Engineering Series; Dover Publications: Mineola, NY, USA, 2007.
6. Guedes Soares, C.; Bhattacharjee, J.; Tello Ruiz, M.; Pietra, L. Review and classification of wave energy converters. In *Maritime Engineering and Technology*; CRC Press: Boca Raton, FL, USA, 2012; pp. 585–594.
7. Falcão, A.F.O. Wave energy utilization: A review of the technologies. *Renew. Sustain. Energy Rev.* **2010**, *14*, 899–918. [[CrossRef](#)]
8. Falnes, J. A review of wave-energy extraction. *Mar. Struct.* **2007**, *20*, 185–201. [[CrossRef](#)]
9. Clément, A.; McCullen, P.; Falcão, A.; Fiorentino, A.; Gardner, F.; Hammarlund, K.; Lemonis, G.; Lewis, T.; Nielsen, K.; Petroncini, S.; et al. Wave energy in europe: Current status and perspectives. *Renew. Sustain. Energy Rev.* **2002**, *6*, 405–431. [[CrossRef](#)]
10. Vicinanza, D.; Di Lauro, E.; Contestabile, P.; Gisonni, C.; Lara, J.L.; Losada, I.J. Review of Innovative Harbor Breakwaters for Wave-Energy Conversion. *J. Waterway Port Coast. Ocean Eng.* **2019**, *145*, 03119001. [[CrossRef](#)]
11. Mendoza, E.; Lithgow, D.; Flores, P.; Felix, A.; Simas, T.; Silva, R. A framework to evaluate the environmental impact of ocean energy devices. *Renew. Sustain. Energy Rev.* **2019**, *112*, 440–449.
12. Falcão, A.F.O.; Henriques, J.C.C. Oscillating-water-column wave energy converters and air turbines: A review. *Renew. Energy* **2016**, *85*, 1391–1424. [[CrossRef](#)]
13. Falcão, A.F.O. First-Generation Wave Power Plants: Current Status and R&D Requirements. In Proceedings of the ASME 22nd International Conference on Offshore Mechanics and Arctic Engineering, Volume 3: Materials Technology, Ocean Engineering, Polar and Arctic Sciences and Technology, Workshops, Cancun, Mexico, 8–13 June 2003; pp. 723–731.
14. Ibarra-Berastegi, G.; Sáenz, J.; Ulazia, A.; Serras, P.; Esnaola, G.; Garcia-Soto, C. Electricity production, capacity factor, and plant efficiency index at the Mutriku wave farm (2014–2016). *Ocean Eng.* **2018**, *147*, 20–29. [[CrossRef](#)]
15. Ning, D.Z.; Wang, R.Q.; Zou, Q.P.; Teng, B. An experimental investigation of hydrodynamics of a fixed OWC Wave Energy Converter. *Appl. Energy* **2016**, *168*, 636–648. [[CrossRef](#)]
16. Chen, J.; Wen, H.; Wang, Y.; Ren, B. Experimental investigation of an annular sector owc device incorporated into a dual cylindrical caisson breakwater. *Energy* **2020**, *211*, 118681. [[CrossRef](#)]
17. Lighthill, J. Two-dimensional analyses related to wave-energy extraction by submerged resonant ducts. *J. Fluid Mech.* **1979**, *91*, 253–317. [[CrossRef](#)]
18. Morris-Thomas, M.T.; Irvin, R.J.; Thiagarajan, K.P. An Investigation Into the Hydrodynamic Efficiency of an Oscillating Water Column. *J. Offshore Mech. Arct.* **2006**, *129*, 273–278. [[CrossRef](#)]
19. Torre-Enciso, Y.; Ortubia, I.; López De Aguilera, L.I.; Marqués, J. Mutriku Wave Power Plant: From the Thinking out to the Reality. In Proceedings of the 8th European Wave and Tidal Energy Conference (EWTEC), Uppsala, Sweden, 7–10 September 2009.
20. Ikoma, T.; Osawa, H.; Masuda, K.; Maeda, H. Expected Values of Wave Power Absorption Around the Japanese Islands Using OWC Types With Projecting Walls. In Proceedings of the ASME 30th International Conference on Ocean, Offshore and Arctic Engineering, Volume 5: Ocean Space Utilization; Ocean Renewable Energy, Rotterdam, The Netherlands, 19–24 June 2011; pp. 573–580.
21. López, I.; Pereiras, B.; Castro, F.; Iglesias, G. Performance of owc wave energy converters: Influence of turbine damping and tidal variability. *Int. J. Energy Res* **2015**, *39*, 472–483. [[CrossRef](#)]
22. John Ashlin, S.; Sannasiraj, S.A.; Sundar, V. Wave Forces on an Oscillating Water Column Device. *Procedia Eng.* **2015**, *116*, 1019–1026. [[CrossRef](#)]
23. John Ashlin, S.; Sundar, V.; Sannasiraj, S. Effects of bottom profile of an oscillating water column device on its hydrodynamic characteristics. *Renew. Energy* **2016**, *96*, 341–353. [[CrossRef](#)]
24. John Ashlin, S.; Sannasiraj, S.A.; Sundar, V. Hydrodynamic performance of an array of oscillating water column device exposed to oblique waves. In Proceedings of the 12th International Conference on Hydrodynamics, Egmond aan Zee, The Netherlands, 18–23 September 2016.
25. Rezanejad, K.; Guedes Soares, C.; López, I.; Carballo, R. Experimental and numerical investigation of the hydrodynamic performance of an oscillating water column wave energy converter. *Renew. Energy* **2017**, *106*, 1–16. [[CrossRef](#)]
26. Howe, D.; Nader, J.R. OWC WEC integrated within a breakwater versus isolated: Experimental and numerical theoretical study. *Int. J. Mar. Energy* **2017**, *20*, 165–182. [[CrossRef](#)]
27. Ashlin, J.S.; Sannasiraj, S.; Sundar, V. Performance of an array of oscillating water column devices integrated with an offshore detached breakwater. *Ocean Eng.* **2018**, *163*, 518–532. [[CrossRef](#)]
28. Rezanejad, K.; Gadelho, J.; Guedes Soares, C. Hydrodynamic analysis of an oscillating water column wave energy converter in the stepped bottom condition using CFD. *Renew. Energy* **2019**, *135*, 1241–1259. [[CrossRef](#)]

29. López, I.; Carballo, R.; Taveira-Pinto, F.; Iglesias, G. Sensitivity of owc performance to air compressibility. *Renew. Energy* **2020**, *145*, 1334–1347. [[CrossRef](#)]
30. Çelik, A.; Altunkaynak, A. Determination of hydrodynamic parameters of a fixed owc by performing experimental and numerical free decay tests. *Ocean Eng.* **2020**, *204*, 106827 [[CrossRef](#)]
31. Chen, J.; Wen, H.; Wang, Y.; Wang, G. A correlation study of optimal chamber width with the relative front wall draught of onshore owc device. *Energy* **2021**, *225*, 120307. [[CrossRef](#)]
32. Qiao, D.; Haider, R.; Yan, J.; Ning, D.; Li, B. Review of Wave Energy Converter and Design of Mooring System. *Sustainability* **2020**, *12*, 8251. [[CrossRef](#)]
33. Medina-Lopez, E.; Allsop, W.; Dimakopoulos, A.; Bruce, T. Conjectures on the Failure of the OWC Breakwater at Mutriku. In Proceedings of the Coastal Structures and Solutions to Coastal Disasters Joint Conference, Boston, MA, USA, 9–11 September 2015.
34. Poullikkas, A. Technology prospects of wave power systems. *Electron. J. Energy Environ.* **2014**, *2*, 47–69.
35. Jin, J.; Liu, Z.; Hyun, B.S.; Hong, K. Effects of wave direction on performance of oscillating water column type wave energy converter. In Proceedings of the International Offshore and Polar Engineering Conference, Rhodes, Greece, 17–22 June 2012; pp. 582–587.
36. Hughes, S.A. *Physical Models and Laboratory Techniques in Coastal Engineering*; World Scientific: Singapore, 1993.
37. Payne, G. *Guidance for the Experimental Tank Testing of Wave Energy Converters*; SuperGen Marine, University of Strathclyde: Glasgow, UK, 2008.
38. Weber, J. Representation of non-linear aero-thermodynamic effects during small scale physical modelling of oscillating water column wave energy converters. In Proceedings of the European Wave and Tidal Energy Conference EWTEC, Porto, Portugal, 11–13 September 2007.
39. Falcão, A.F.O.; Henriques, J.C. Model-prototype similarity of oscillating-water-column wave energy converters. *Int. J. Mar. Energy* **2014**, *6*, 18–34. [[CrossRef](#)]
40. Sarmiento, A.J.N.A. Model-Test Optimization of an Owc Wave Power Plant. *Int. J. Offshore Polar Eng.* **1993**, *3*, ISOPE-93-03-1-066.
41. Medina Rodríguez, A.A.; Blanco Ilzarbe, J.M.; Silva Casarín, R.; Izquierdo Ereño, U. The Influence of the Chamber Configuration on the Hydrodynamic Efficiency of Oscillating Water Column Devices. *J. Mar. Sci. Eng.* **2020**, *8*, 751. [[CrossRef](#)]
42. Medina Rodríguez, A.A.; Silva Casarín, R.; Blanco Ilzarbe, J.M. The influence of oblique waves on the hydrodynamic efficiency of an onshore owc wave energy converter. *Renew. Energy* **2022**, *183*, 687–707. [[CrossRef](#)]
43. He, G.; Huang, Z. Using an Oscillating Water Column Structure to Reduce Wave Reflection from a Vertical Wall. *J. Waterw. Port Coast. Ocean Eng.* **2016**, *142*, 04015021. [[CrossRef](#)]
44. Iturrioz, A.; Guanche, R.; Lara, J.L.; Vidal, C.; Losada, I.J. Validation of OpenFOAM® for Oscillating Water Column three-dimensional modeling. *Ocean Eng.* **2015**, *107*, 222–236. [[CrossRef](#)]
45. Howe, D.; Nader, J.R.; Macfarlane, G. Experimental investigation of multiple Oscillating Water Column Wave Energy Converters integrated in a floating breakwater: Energy extraction performance. *Appl. Ocean Res.* **2020**, *97*, 102086. [[CrossRef](#)]
46. Ning, D.Z.; Shi, J.; Zou, Q.P.; Teng, B. Investigation of hydrodynamic performance of an OWC (oscillating water column) wave energy device using a fully nonlinear HOBEM (higher-order boundary element method). *Energy* **2015**, *83*, 177–188. [[CrossRef](#)]
47. Kamath, A.; Bihs, H.; Arntsen, Ø.A. Numerical investigations of the hydrodynamics of an oscillating water column device. *Ocean Eng.* **2015**, *102*, 40–50. [[CrossRef](#)]